Search for the Lepton Flavour Violating Decay tau→e gamma

by

Clayton Daniel Lindsay
B.Sc., University of Victoria, 2007

A Thesis Submitted in Partial Fulfillment of the

Requirements for the Degree of
MASTER OF SCIENCE
in the Department of Physics and Astronomy

Search for the Lepton Flavour Violating Decay tau→e gamma

by

Clayton Daniel Lindsay
B.Sc., University of Victoria, 2007

Supervisory Committee

Dr. J. Roney, Supervisor (Department of Physics and Astronomy)

Dr. A. Ritz, Member (Department of Physics and Astronomy)

Supervisory Committee

Dr. J. Roney, Supervisor (Department of Physics and Astronomy)

Dr. A. Ritz, Member (Department of Physics and Astronomy)

Abstract

A search is done on the entire *BABAR* data set for the neutrino-less τ decay $\tau^{\pm} \rightarrow e^{\pm}\,\gamma$. No evidence for the decay is found and a 90% confidence level upper limit is determined to be 3.3×10^{-8} including systematic uncertainty. This measurement is a factor of three improvement from the previous best result from *BABAR* .

Table of Contents

List of Tables

List of Figures

Acknowledgements

I'd like to acknowledge Dr. Swagato Banerjee and Dr. Mike Roney for their support in completing this thesis.

Chapter 1

Introduction

The Standard Model (SM) of particle physics has reigned as the prevailing theory of particle physics for the past forty years. Finally toppled by the discovery of neutrino oscillations, the Standard Model may soon be replaced with a new theory of particle physics. Tests of lepton flavour violation in the charged sector could be pivotal in ruling out new theoretical models. This thesis discusses the search for the lepton flavour violating decay $\tau^{\pm} \to e^{\pm}\,\gamma$ in the *BABAR* experiment.

Constructed to study CP violation in the $B^0\bar{B}^0$ system, the *BABAR* detector collects information from positron-electron collisions provided by the PEP-II storage rings located at the SLAC National Accelerator Laboratory. Between 1999 and 2008, *BABAR* has recorded nearly half a billion tau pairs from decaying $\Upsilon(2S)$, $\Upsilon(3S)$ and $\Upsilon(4S)$ resonant quark states. Measurements of the branching fraction for $\tau^{\pm} \to e^{\pm}\,\gamma$ have been done [1], using approximately half of the *BABAR* data set, resulting in a fraction consistent with zero. From the measurement a 90% confidence level upper limit of $1.1 \cdot 10^{-7}$ was assigned. The purpose of this work is to search the full *BABAR* data set for this rare decay and measure a branching fraction or improve the previous upper limit.

Chapter 2 discusses the SM, its particle content, lepton flavour violation and

experimental methods for approximating the branching ratio. Chapter 3 details the *BABAR* hardware and trigger system. Chapter 4 describes the selection process and the requirements placed on the data to separate signal decays from backgrounds. Chapters 5 and 6 discuss experimental systematic uncertainties and the results of the analysis respectively.

Chapter 2

Theory

This thesis begins by introducing the Standard Model (SM) of particle physics and its particle constituents. Details follow on the electro-weak interaction and the τ lepton. The concept of lepton flavour and its violation are discussed, which motivates a theory beyond the SM. Lastly statistical methods used in a search for $\tau^{\pm} \to e^{\pm}\,\gamma$ are defined. This thesis uses 'natural units' wherein the speed of light, c, and Planck's constant, $\hbar$, are equal to one.

2.1 The Standard Model

All known interactions in the universe can be classified as one of the four fundamental forces: electromagnetic, weak, strong and gravity. The first two of these forces are well described and calculable under electro-weak theory (EWT). The strong force is described by Quantum Chromodynamics (QCD); but, in low energy cases, is too complex to calculate. Gravity has yet to be successfully quantized. The SM combines EWT and QCD into a very successful theory of particle interactions.

In the SM, all matter is composed of fundamental spin[1] $\frac{1}{2}$ particles known as leptons and quarks. There are six[2] leptons that come in three flavours: electron,

[1] Spin is the intrinsic component of a particle's angular momentum.

[2] There are also six anti-leptons, having the opposite charge of their corresponding leptons.

	Symbol	Charge	Mass
electron	e	-1	0.511 MeV
electron neutrino	ν_e	0	< 2 eV
muon	μ	-1	105.7 MeV
muon neutrino	ν_μ	0	< 0.17 MeV
tau	τ	-1	1.777 GeV
tau neutrino	ν_τ	0	< 15.5 MeV

Table 2.1: Properties of the six leptons grouped by flavour. Not shown are the anti-leptons which have the same mass and opposite charge of their corresponding leptons.

	Symbol	Charge	Mass
up	u	2/3	1.5-3.3 MeV
down	d	$-1/3$	3.5-6.0 MeV
strange	s	$-1/3$	70-130 MeV
charm	c	2/3	1.16-1.34 GeV
bottom	b	$-1/3$	4.13-4.37 GeV
top	t	2/3	171 ± 1.6 GeV

Table 2.2: Properties of the six quarks by generation. Not shown are the anti-quarks which have the same mass and opposite charge of their corresponding quarks.

muon and tau. Charged leptons interact via the electromagnetic and weak forces; neutral leptons interact only weakly. Table 2.1 shows the six leptons and some of their properties.

In addition to electromagnetic and weak, the 6 quarks interact via the strong force. Each quark carries 'colour charge', analogous to electric charge, which is associated with the strong force. There are three colours and quarks are confined to composite colour- neutral particles[3] known as hadrons. The quarks are divided into 3 generations increasing in mass. Table 2.2 shows the six quarks and some of their properties.

[3]A colour neutral particle is composed of either one of each red, green, blue quarks (baryons) or a colour/anti-colour pair (mesons).

	Symbol	Force	Charge	Mass
photon	γ	Electromagnetism	0	0
gluon	g	Strong	0	0
W boson	$W^{\pm}$	Weak	± 1	$80.40 \pm 0.04\,\mathrm{GeV}$
Z boson	Z^0	Weak	0	$91.188 \pm 0.002\,\mathrm{GeV}$

Table 2.3: Properties of the 4 mediator particles.

The spin one force mediator bosons[4] are responsible for all interactions between the quarks and leptons. The electromagnetic force is mediated by the neutral photon. The weak force is mediated by the charged $W^{\pm}$ and neutral Z bosons. The strong force is mediated by the colour charged gluons. Table 2.3 shows some properties of the force mediator particles.

2.2 The Weak Interaction and Lepton Flavour

As the name suggests, the weak interaction is orders of magnitude weaker than the strong and electromagnetic forces. In fact, the weak interaction is difficult to detect unless the strong and electromagnetic are highly suppressed.

One unique characteristic of the weak force is its flavour manipulation properties. For example, the neutron may undergo 'beta decay' where it decays into a proton, electron and anti-neutrino. Through this weak interaction, the quark changes flavour from down to up which is not possible in an electromagnetic or strong interaction.

Interactions in quantum field theories can be conveniently represented by Feynman diagrams. The example of beta decay is shown in Figure 2.1. One can interpret these diagrams as time progressing from left to right.

The result is the initial neutron decays into a proton, electron and an anti-neutrino. Not only are these diagrams visually instructive, they also serve to calculate

[4]Bosons are particles with integer spin.

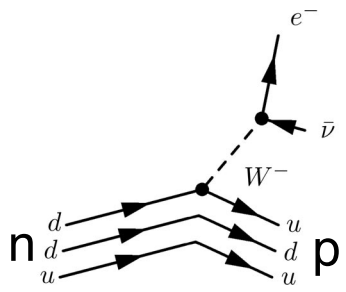

Figure 2.1: Feynman diagram of beta decay: $n \rightarrow p^+ e^- \bar{\nu}_e$. Interpreted as time progressing left to right: initially there is a neutron, a down quark within the neutron weakly decays to an up quark and a W boson, W boson propagates and interacts weakly producing an anti-neutrino and electron.

the probability that the interaction will occur. Each diagram represents a term in the 'S matrix' expansion where, given initial and final particle states $\langle i|$ and $|f\rangle$, the probability of the interaction is $|\langle i|S|f\rangle|^2$.

While the weak interaction is able to modify the flavour of the quarks as in beta decay, the SM does restrict all interactions based on initial and final particle flavour. One such restriction is known as lepton flavour conservation:

$$L_\ell = n_\ell - n_{\bar{\ell}}$$

$\mathbf{L}_\ell$	conserved flavour number for $\ell \in (e, \mu\tau)$
$\mathbf{n}_\ell$	number of leptons of flavour $\ell \in (e, \mu, \tau)$
$\mathbf{n}_{\bar{\ell}}$	number of anti-leptons of flavour $\ell \in (e, \mu, \tau)$

For each flavour of lepton, the number of leptons minus the number of anti-leptons is constant throughout any Standard Model interaction.

An example of this conservation is the beta decay from Figure 2.1. The initial neutron has an electron flavour number of zero ($L_\ell = 0$). After the interaction the the flavour number of the proton, electron and anti-electron neutrino remains zero ($L_\ell = 1 - 1 = 0$).

2.3 The Tau Lepton

The most massive of the leptons is the tau at 1.777 GeV. Discovered in 1975 at the Stanford Linear Accelerator, the tau's existence was inferred by the number of missing particles in the interaction:

$$e^+e^- \rightarrow e^\pm\mu^\mp + \text{at least 2 invisible} \tag{2.1}$$

$$\Rightarrow\ e^+e^- \rightarrow \tau^+\tau^- \rightarrow e^\pm\mu^\mp\ \nu_\tau\ \bar{\nu}_\tau\ \nu_e\ \nu_\mu \tag{2.2}$$

Momentum and energy conservation necessitated at least 2 invisible particles in (2.1) above. The creation of a tau pair was postulated as in (2.2) and later confirmed.

The tau is unstable and readily decays weakly to both hadrons and leptons. Many decay modes are possible including those with one, three, and five charged particles. Define Γ_i, the decay rate of the i^{th} mode, as the probability per unit time that the tau will undergo this decay. The total probability per unit time of decay is then:

$$\Gamma_{tot} = \sum_i \Gamma_i$$

The mean lifetime is then the reciprocal of this total decay rate: $\mathcal{T} = 1/\Gamma_{tot}$. The tau decays too quickly to directly detect experimentally with a mean lifetime of 290 ± 1 femtoseconds [2]. The presence of the tau is always inferred in experiment.

One final useful quantity when discussing tau decays is a decay 'branching fraction', denoted $\mathcal{B}$ and defined as:

$$\mathcal{B}(i^{th}\text{decay mode}) = \frac{\Gamma_i}{\Gamma_{tot}}$$

Given a decaying tau, the branching fraction of a mode is the probability that the

Decay Mode	Branching Fraction (10^{-2})
$\tau^- \rightarrow \pi^-\pi^0\nu_\tau$	25.51 ± 0.09
$\tau^- \rightarrow e^-\bar{\nu}_e\nu_\tau$	17.85 ± 0.05
$\tau^- \rightarrow e^-\bar{\nu}_e\nu_\tau\gamma$	1.75 ± 0.18
$\tau^- \rightarrow \mu^-\bar{\nu}_\mu\nu_\tau$	17.36 ± 0.05
$\tau^- \rightarrow \mu^-\bar{\nu}_\mu\nu_\tau\gamma$	0.36 ± 0.04
$\tau^- \rightarrow \pi^-\nu_\tau$	10.91 ± 0.07
$\tau^- \rightarrow \pi^-\pi^-\pi^+\nu_\tau$	9.32 ± 0.07
$\tau^- \rightarrow \pi^-2\pi^0\nu_\tau$	9.29 ± 0.11

Table 2.4: Some common decay modes [2] for the τ lepton. Charge conjugated decay modes are identical with all charge signs switched.

tau will decay via this mode. Table 2.4 shows some common tau decay modes and their branching fractions.

2.4 Lepton Flavour Violation

The SM has been extremely successful as a theory of particle physics. Until 2001 and the measurement of neutrino oscillations [3] [4] [5], every experimental test had been consistent with the SM which was conceived in 1960's. The discovery that neutrinos may spontaneously change flavour disproved the conservation of lepton flavour and implied that neutrinos had a non-zero mass. A straight-forward method for the addition of neutrino oscillation to the SM involves adding a leptonic mixing matrix such that leptons are able to change flavour in a similar fashion to quarks. While this rectifies the discrepancy, non-conservation of lepton flavour is a signature of some new particle physics theories.

With the addition of a leptonic mixing matrix which allows neutrino mixing to the SM, it is not only possible for neutrinos to oscillate, but also charged leptons. Figure 2.2 shows a potential diagram, including an oscillating neutrino, for the decay

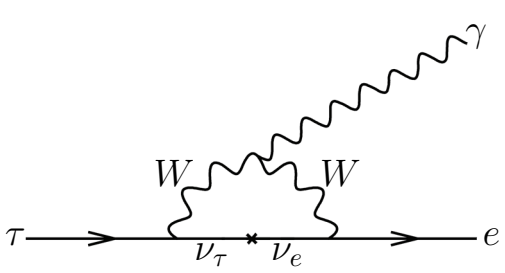

Figure 2.2: Feynman diagram for $\tau^{\pm} \rightarrow e^{\pm}\,\gamma$ including an oscillating neutrino.

$\tau^{\pm} \rightarrow e^{\pm}\,\gamma$. This neutrino-less tau decay violates lepton flavour conservation and is allowed in the SM augmented with lepton mixing. The decay rate due to this diagram has been calculated [6] giving the proportionality:

$$\Gamma(\tau^{\pm} \rightarrow e^{\pm}\,\gamma\,) \propto \left(\frac{\Delta m_{\nu}^2}{m_W^2}\right)^2 \times \Gamma(\tau \rightarrow e\;\bar{\nu}_e\;\nu_\tau)$$

$\mathbf{\Delta m_\nu}$	$m^2_{\nu_\tau} - m^2_{\nu_e}$
$\mathbf{m_W}$	mass of W boson $\approx 80\,\mathrm{GeV}$

Combined with the result from neutrino oscillation experiments [5] $\Delta m_{\nu}^2 \sim 3 \times 10^{-3}(\,\mathrm{eV}^2)$, this gives:

$$\Gamma(\tau^{\pm} \rightarrow e^{\pm}\,\gamma\,) \approx (10^{-54}) \times \Gamma(\tau \rightarrow e\;\bar{\nu}_e\;\nu_\tau)$$

This result for SM lepton flavour violation is far too small to be detected in modern particle physics experiments.

Experimental evidence of a branching fraction for $\tau^{\pm} \rightarrow e^{\pm}\,\gamma$ well above the SM prediction would be a clear sign of new physics. While neutrino oscillation has already forced an augmentation of the SM, charged lepton flavour violation could not so easily be remedied. Some new theories of physics, such as supersymmetric (SUSY) models [7], predict charged lepton flavour violating branching fraction as high as $\mathcal{B} \sim 10^{-7}$, making a search for $\tau^{\pm} \rightarrow e^{\pm}\,\gamma$ useful in constraining new models.

SUSY postulates that every known particle has a 'superpartner' particle. Every boson has a superpartner fermion; every fermion has a superpartner boson. These SUSY particles are massive and out of experimental reach for direct detection. However, it is pos-

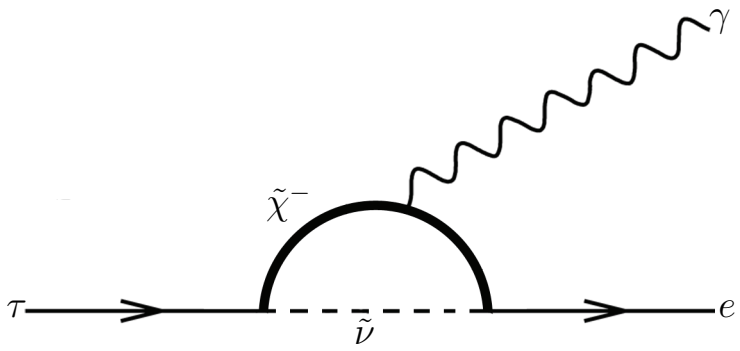

(a) SUSY diagram for $\tau^{\pm} \rightarrow e^{\pm}\ \gamma$ with charginos ($\tilde{\chi}^-$) and sneutrinos ($\tilde{\nu}$).

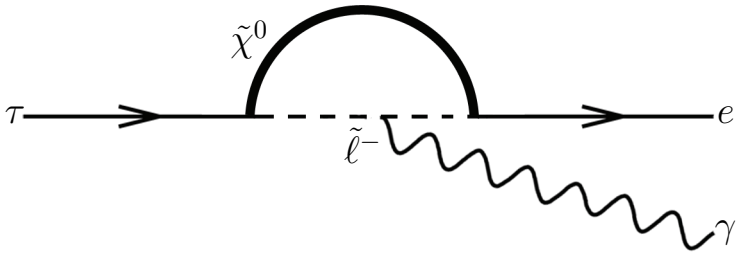

(b) SUSY diagram for $\tau^{\pm} \rightarrow e^{\pm}\ \gamma$ with neutralinos ($\tilde{\chi}^0$) and charged sleptons ($\tilde{\ell}^-$).

Figure 2.3

sible to infer the existence of such particles by their contributions to loop diagrams. Two such diagrams produce LFV as shown in Figures 2.3a and 2.3b. These diagrams contain lepton superpartners (sleptons and sneutrinos) and generic charged and neutral particles (charginos and neutralinos).

Minimal Super Gravity (mSUGRA) is a widely investigated minimal extension of the SM which realizes SUSY. Some parameters for this theory, such as the masses of the sneutrinos, are estimated using both cosmological and high energy physics constraints. Other parameters, such as the universal scalar and gaugino[5] masses, M_0 and $M_{1/2}$, must be constrained by modern experiments. LFV is present in some theories [7] – Figures 2.4a and 2.4b show the predicted branching fraction for two configurations of an mSUGRA theory. The complex angle θ_1 of the diagrams is one parameter in a 3×3 orthogonal matrix

[5]Gauginos are the proposed super partners of gauge bosons.

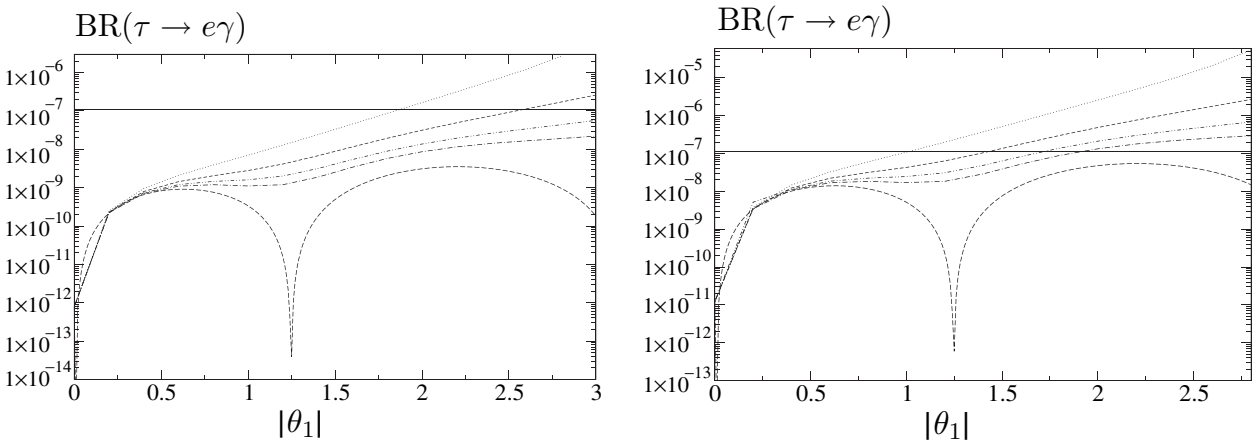

(a) $\tau^{\pm} \to e^{\pm}\,\gamma$ branching fraction for mSUGRA with $M_0 = 400\,\text{GeV}$, $M_{1/2} = 300\,\text{GeV}$ [7]

(b) $\tau^{\pm} \to e^{\pm}\,\gamma$ branching fraction for mSUGRA with $M_0 = 250\,\text{GeV}$, $M_{1/2} = 150\,\text{GeV}$ [7]

Figure 2.4: $\tau^{\pm} \to e^{\pm}\,\gamma$ branching ratio vs θ_1 magnitude for an mSUGRA based model [7]. The dotted lines indicate the phase of θ_1 (0, $\pi/10$,$\pi/8$,$\pi/6$,$\pi/4$ radians from bottom to top).

which relates the masses of the neutrinos to their sneutrino partners. The horizontal axis shows the magnitude and the dotted lines show the phase (0, $\pi/10$,$\pi/8$,$\pi/6$,$\pi/4$ radians from bottom to top). The previous experimental limit is shown as a solid horizontal line.

A more strict upper limit on $\tau^{\pm} \to e^{\pm}\,\gamma$ would constrain this θ_1 parameter as well as the 'SUSY breaking' masses M_0 and $M_{1/2}$.

2.5 Search for Neutrino-less τ Decay

The *BABAR* experiment, which observes τ pairs produced from e^+e^-collisions (Figure 2.5), has the potential to search for a τ branching fraction as small as 10^{-8}. Using the large volume of data available from *BABAR*, an experimental branching fraction for $\tau^{\pm} \to e^{\pm}\,\gamma$ may be determined as:

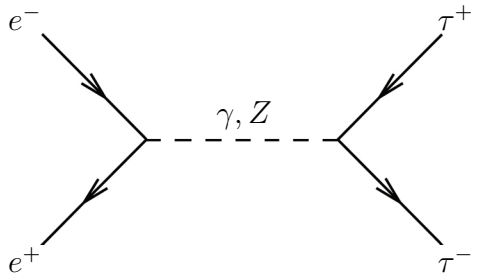

Figure 2.5: Feynman diagram of τ pair production: $e^+e^- \rightarrow \tau^+\tau^-$

$$\mathcal{B}_{exp}(\tau^\pm \rightarrow e^\pm\, \gamma\,) = \frac{N_{sel}}{N_{decay}} = \frac{N_{sel}}{2N_{\tau^+\tau^-}}$$

$\mathbf{N_{sel}}$	Number of observed $\tau^\pm \rightarrow e^\pm\, \gamma$ decays
$\mathbf{N_{decays}}$	Total number of τ decays analyzed
$\mathbf{N_{\tau^+\tau^-}}$	Number of τ pairs analyzed

As the number of τ pairs analyzed increases to infinity, it is expected that this experimental branching fraction will converge to the actual branching fraction.

While it would be ideal to single out $\tau^\pm \rightarrow e^\pm\, \gamma$ decays (signal decays), in practicality the *BABAR* detector is unable to discern these signal decays from several other dominant SM decays. Such decays which are difficult to separate from signal are known as backgrounds. Some of the dominant backgrounds in a search for $\tau^\pm \rightarrow e^\pm\, \gamma$ at *BABAR* are shown in Figures 2.6 and 2.7. All of these events appear similar in the detector and are challenging to separate from signal.

In addition, it is not possible to analyze all of the potential signal decays due to experimental limitations in hardware and software. The best that can be done is determine an efficiency ($\epsilon = N_{sel}^{sig}/N_{tot}$) with which the signal events are selected.

The real experimental branching fraction that may then be measured is:

$$\mathcal{B}_{exp}(\tau^\pm \rightarrow e^\pm\, \gamma\,) = \frac{N_{sig} - N_{bkg}}{2N_{\tau^+\tau^-}\epsilon}$$

$\mathbf{N_{sig}}$	Number of signal events selected
$\mathbf{N_{bkg}}$	Number of background events selected
ϵ	Signal selection efficiency

It may be that no signal decays are found within the *BABAR* dataset, it is still possible

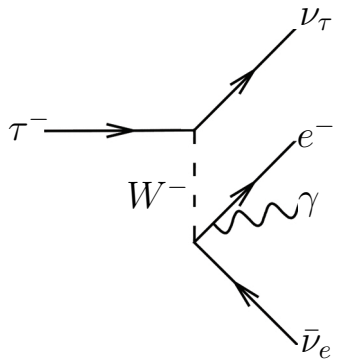

Figure 2.6: Leptonic tau decay with final state radiation: $\tau^- \to e^- \nu_\tau \bar{\nu}_e \gamma$

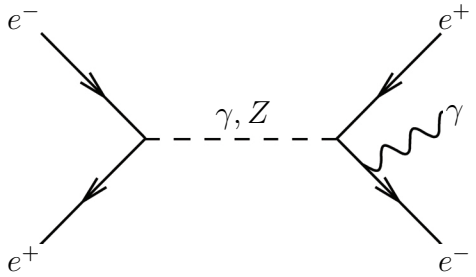

Figure 2.7: Bhabha process with final state radiation $e^+e^- \to e^+e^- \to e^+e^-\gamma$

to extract useful information from a search. A 90% confidence level (CL) upper limit (UL) on the branching fraction may be set using the method of Feldman and Cousins [8]. It is assumed that all selected events are backgrounds. The 90% CL ensures that 90% of experiments will yield a branching fraction lower than the UL calculated as:

$\mathbf{N_{signal}^{90\%CL}}$	Number of signal events for Feldman-Cousins 90% CL UL [8] assuming no signal

$$\mathcal{B}_{90\%CL}(\tau^\pm \to e^\pm \gamma\ ) = \frac{N_{signal}^{90\%CL}}{2N_{\tau^+\tau^-}\epsilon} \qquad (2.3)$$

This upper limit may then be used to place constraints on new physics models.

Chapter 3

Detector

3.1 The PEP-II Accelerator

PEP-II is an accelerator located at the SLAC National Accelerator Laboratory on the Stanford University campus. Constructed to study CP violation in B^0 decays, PEP-II is composed of two storage rings as shown in Figure 3.1. Low energy electrons from an electron gun are inserted at one end of a 3km long linear accelerator (linac). These electrons are accelerated through the machine to an energy of 9.1 GeV and then extracted to one of the two PEP-II storage rings. Along the way some electrons are extracted and run through a tungsten-rhenium target – producing positrons. The positrons are then focussed and re-inserted into the linac, accelerated to 3.0 GeV and extracted into the second storage ring [9].

The two beams are collided head-on resulting in an energy of 10.58 GeV in the centre of mass frame (CM). This energy coincides with the $\Upsilon(4S)$ resonant $b\bar{b}$ quark state which is ideal for the study of B^0 mesons as $\Upsilon(4S)$ lies just above the $B^0\bar{B}^0$ threshold. $\Upsilon(4S)$ decays to $B^0\bar{B}^0$ greater than 96% of the time [2] with too little remaining energy to produce any excess pions which could complicate the sample. As PEP-II is designed to search for rare CP violating decays, it must provide a high luminosity of $10^{34} cm^{-2} s^{-1}$. The number of

Interaction	Cross-section (nb)
$e^+e^- \to b\bar{b}$	1.05
$e^+e^- \to c\bar{c}$	1.30
$e^+e^- \to s\bar{s}$	0.35
$e^+e^- \to u\bar{u}$	1.39
$e^+e^- \to d\bar{d}$	0.35
$e^+e^- \to \tau^+\tau^-$	0.94
$e^+e^- \to \mu^+\mu^-$	1.16
$e^+e^- \to e^+e^-$	~ 40

Table 3.1: e^+e^-cross-sections expected with CM energy of 10.58 GeV at PEP-II [9].

particles created is the product of the integrated luminosity and cross-section for the process which creates the particle in question.

Table 3.1 indicates that the cross-section for τ lepton production is only slightly smaller than B meson production; hence, PEP-II produces roughly the same number of τ and B particles. The high luminosity combined with large cross-section for τ production provides an excellent environment for rare decay searches such as $\tau^\pm \to e^\pm\,\gamma$.

3.2 The BaBar Detector

The BaBar detector is situated at the interaction point (IP) of the beams provided by PEP-II. Its purpose is to determine the characteristics of interesting interactions that occur as a result of the e^+e^-collisions. BaBar, shown in Figure 3.2, employs a coordinate system wherein the z-axis is aligned with the e^- beam, the y-axis points vertically and the x-axis points toward the inside of the PEP-II storage rings. Most often used throughout this analysis are spherical coordinates wherein the x and y coordinates are replaced with θ and ϕ which represent the polar angle from the z-axis and the x-y planar azimuth respectively.

BaBar is asymmetric as the two beam energies are different. Hence, considering cost restraints, it is worthwhile to better instrument the forward region[1] of the detector due to

[1]Forward is defined as downstream of the e^- beam

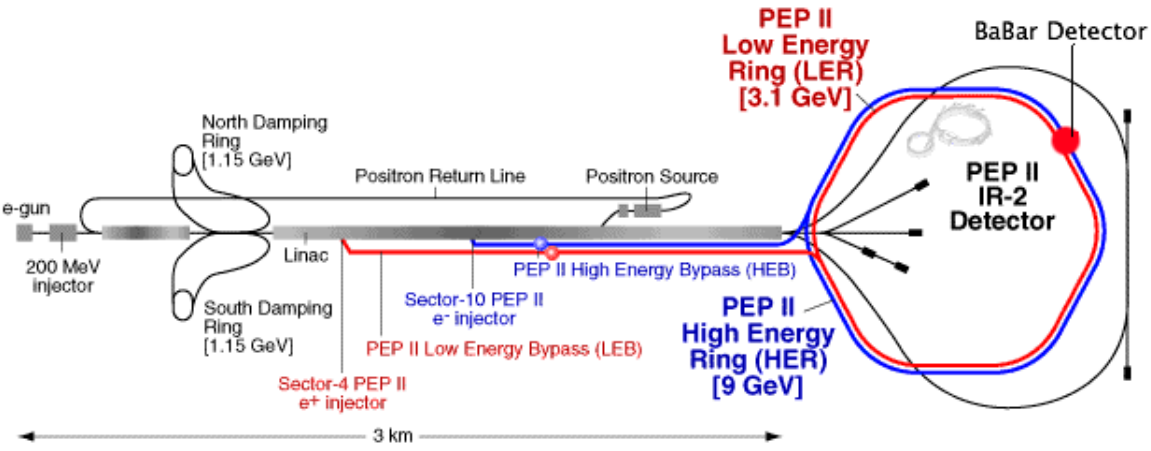

Figure 3.1: Diagram of the PEP-II accelerator [10, BaBar Detector Image Gallery]

the higher particle flux.

Increasing in radial distance from the IP the five main components of the BaBar detector: the silicon vertex tracker (SVT), the drift chamber (DCH), the detector of internally reflected Cherenkov light (DIRC), the electromagnetic calorimetry (EMC) and the instrumented flux return (IFR). In addition, BaBar uses a superconducting solenoid magnet to provide a 1.5 Tesla magnetic field parallel to the beam axis. The field forces charged particles into a curved trajectory which allows for momentum measurements

3.2.1 Silicon Vertex Tracker

The SVT sits at the centre of the detector and is primarily used for precisely determining initial charged particle trajectories and interaction vertices. In addition, all tracking[2] information for particles with transvers momentum[3] (p_t) less than 100 MeV must be provided by the SVT [12]. Located closest to the beamline at the centre of the detector, the SVT

[2]Tracking refers the determination of the trajectory of a charged particle through the detector.
[3]p_t is the component of a particle's momentum transverse to the z-axis.

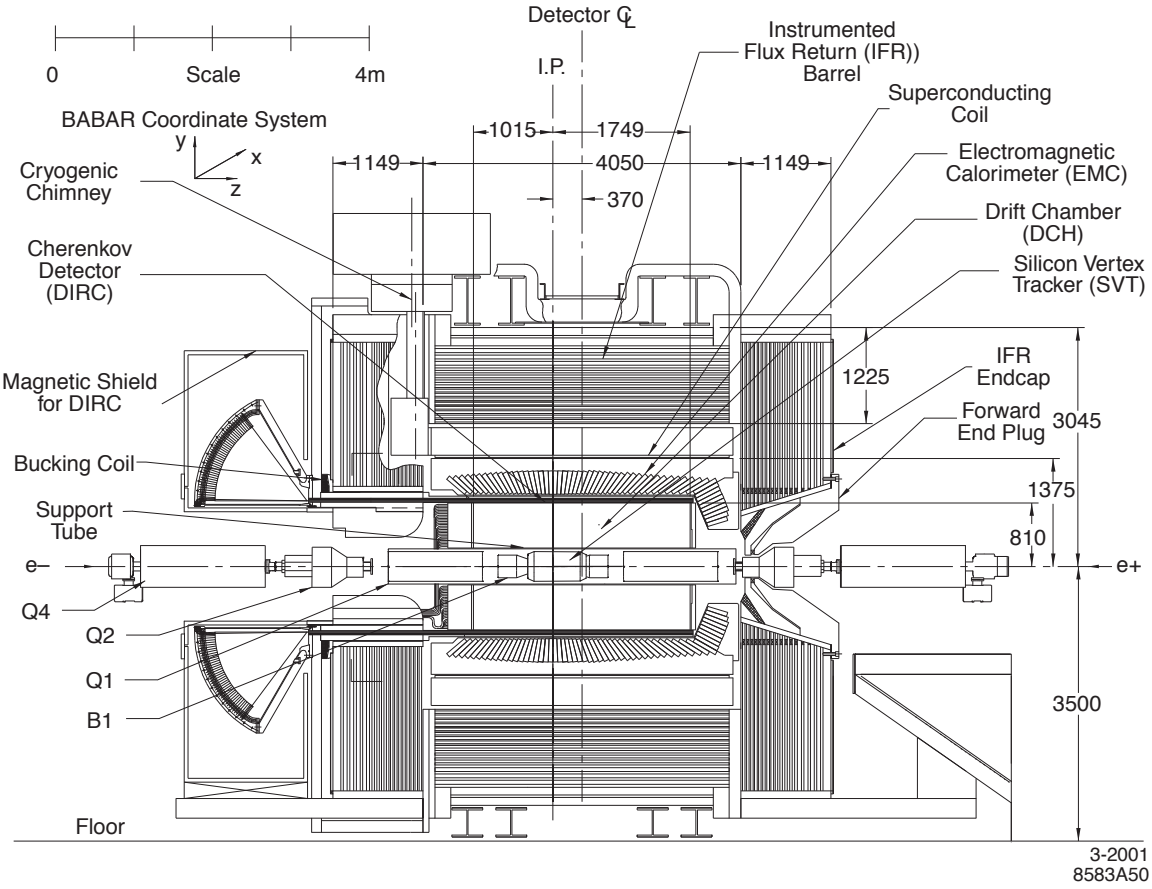

Figure 3.2: Schematic of the BaBar detector [11]

is exposed to more radiation than any other BaBar component; hence, it must be very radiation hard. In addition, an accurate measurement of the vertex requires minimization of multiple Coulomb scattering; hence, a low atomic mass (Z) material is needed.

Schematics of the beam-parallel and x-y plane SVT geometry are shown in Figures 3.3 and 3.4 respectively. The material of the detector is dictated largely by the fact that it must be radiation hard. Silicon strips were chosen as they provide acceptable radiation hardness, are relatively inexpensive, light weight and can provide the necessary position resolution for CP violating B^0 studies. Double sided strips readout the z and ϕ coordinates while the radial (and hence θ) is determined by having a five layered device.

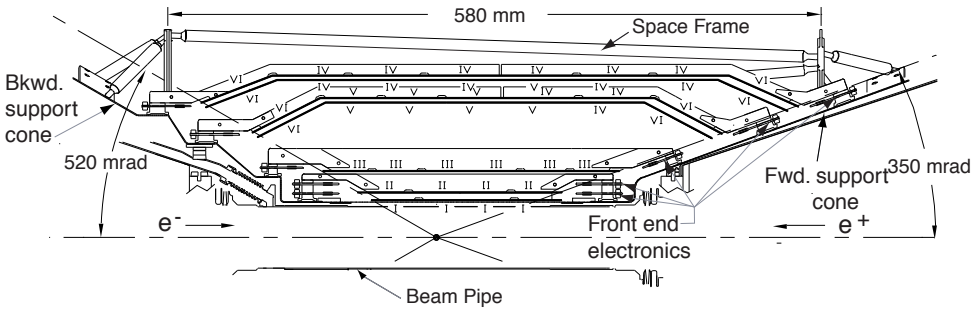

Figure 3.3: Schematic of a z-axis parallel section of the SVT [11]

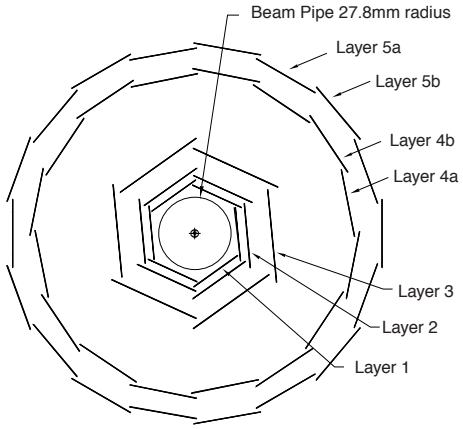

Figure 3.4: Schematic of a x-y plane section of the SVT [11]

3.2.2 Drift Chamber

The main purposes of the DCH is to provide accurate momentum and tracking information for charged particles. In addition, the DCH is fast enough to provide Level 1 trigger information. For the case of low momentum particles, the DCH provides particle ID via ionization energy loss (dE/dx) measurements. In order to complement the SVT measurement, it is again necessary to have a low Z material to avoid multiple Coulomb scattering.

Figure 3.5a shows a beam-parallel section of the DCH. High voltage gold-plated tungsten 'sense' wires are strung axially along the detector enclosed within a Helium/isobutane gas. Figure 3.5b shows a section of the DCH wire geometry. Wires are placed in a regular

pattern and produce a well-mapped electric field. Charged particles passing through the DCH ionize the gas producing electrons which drift in the electric field toward the sense wires. As the electrons approach the wires they accelerate causing an 'avalanche'[4] effect which produces a detectable signal on the wires. The timing of the avalanche on the wires is used to reproduce charge particle trajectories through the chamber. Each sensor wire is surrounded by a hexagon of field wires and is collectively known as a cell. Forty cells are stacked radially outward with wires stretching parallel to the beam axis symmetrically in ϕ. Cell size and configuration was optimized for $B^0 \to \pi^+ \pi^-$ mass resolution [12].

The track parameters ϕ, curvature and radius are determined by ionization on the axial wires. The remaining parameters z, θ are determined by using a scheme of angled wires. The DCH wire layers alternate between angled ($\pm 50 mrad$) and beam-axis parallel orientations. Using the variation in drift time over the length of the detector, the z and θ coordinates may be extracted. This approach for the z coordinate allows a minimal amount of material to be present within the active region.

Experimentally the momentum resolution of the DCH has been determined to be [11]:

$$\frac{\sigma_{p_t}}{p_t} = (0.13 \pm 0.01)\% \times p_t + (0.45 \pm 0.03)\%$$

The drift chamber also makes a measurement of particle energy loss (dE/dx) by determining the energy deposited through the ionizaiton process. A measurement of dE/dx allows for a calculation of the charged particle's velocity (β) via the Bethe-Bloch equation [2].

3.2.3 Detector of Internally Reflected Cherenkov Light

Knowing the velocity (β) and momentum of a particle allow for the determination of its mass. Charged pions and kaons leave similar signatures within the BaBar detector; but,

[4]Electrons acclerated toward the wires in the gas cause more electrons to be ionized from the gas – the result is an 'avalanche' of electrons increasing in number near the wires.

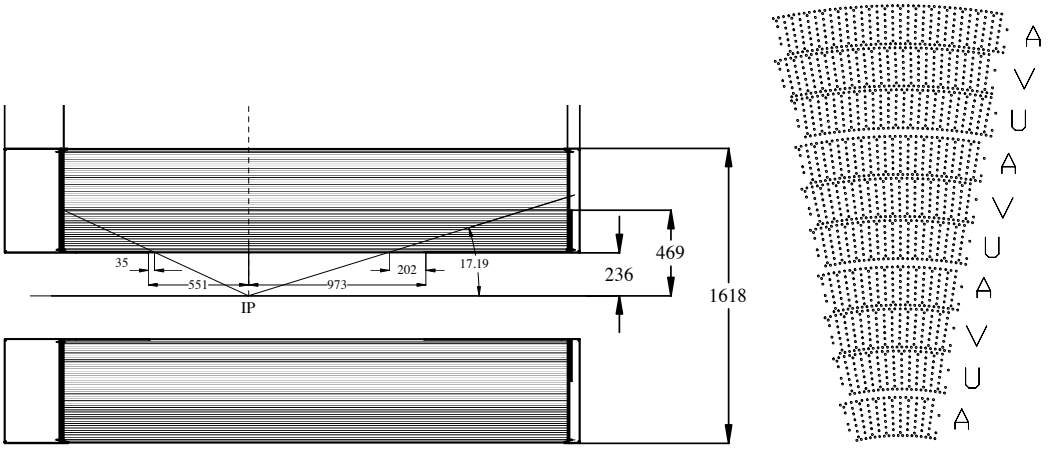

(a) Beam parallel section schematic of the DCH [11]

(b) x-y section of the DCH wire geometry.

Figure 3.5

they differ greatly in mass. Hence it is useful to combine the momentum measurement from the DCH with an independent measurement of velocity to determine the mass. The DIRC provides the independent velocity measurement through the use of Cherenkov light.

When a charged particle exceeds the speed of light within some medium, it may emit a ring of photons known as Cherenkov light. The DIRC consists of a layer of quartz bars surrounding the DCH. Charged particles passing through the quartz are sufficiently fast to produce a ring of Cherenkov photons. These photons then undergo internal reflection within the bar and propagate to a wall of photomultiplier tubes contained in a tank of high purity water as shown in Figure 3.6. The photon positions along with the initial position of the charged track is used to determine the angle of the Cherenkov photons. This angle then gives a measurement of β as $cos\theta_C = \frac{1}{n\beta}$ where n is the index of refraction of the quartz. The DIRC allows for excellent kaon/pion separation within a 500MeV - 4.5GeV range [11].

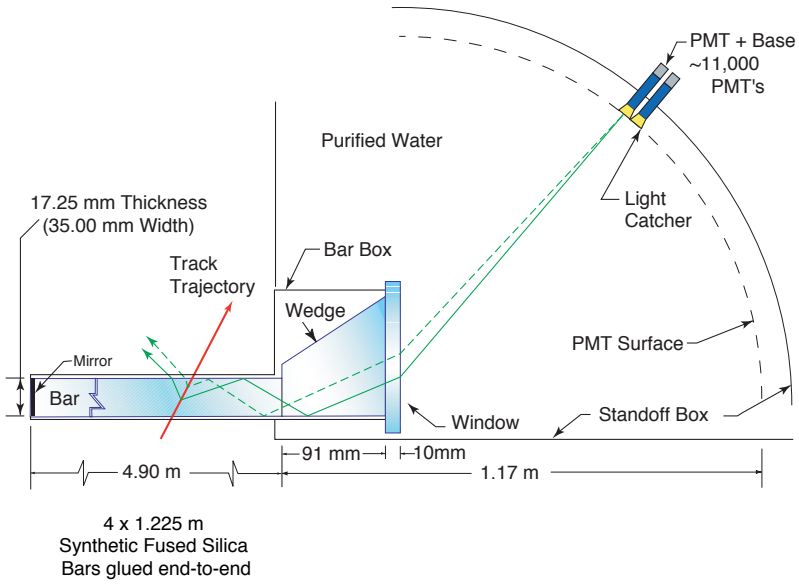

Figure 3.6: Illustration of principle upon which the detector of internally reflected Cherenkov light is based. [10]

3.2.4 Electromagnetic Calorimetry

The BaBar electromagnetic calorimeter (EMC) encloses the DIRC system. EMC is tasked with measuring the energy of electrons and photons, the direction of neutral hadrons and provides discrimination between electrons and charged hadrons[5].

At high energy (much larger than characteristic atomic energies) electrons primarily deposit energy into material via Bremsstrahlung which produces a photon. Above e^+e^- threshold photons mainly deposit energy via pair production producing electrons and positrons. These are the main mechanisms by which electrons and photons deposit their energy in the EMC. An electron or photon enters and undergoes Bremsstrahlung or pair production producing more electrons and photons. This process continues until the resultant electrons and photons are slowed enough to be absorbed by atoms. The result is an 'electromagnetic shower' of photons and electrons as depicted in Figure 3.7 (right).

CsI(Tl) crystals are used in the BaBar EMC to force photons and electrons to shower.

[5]Electrons and hadrons seperated through a measurement of Energy/momentum (E/p).

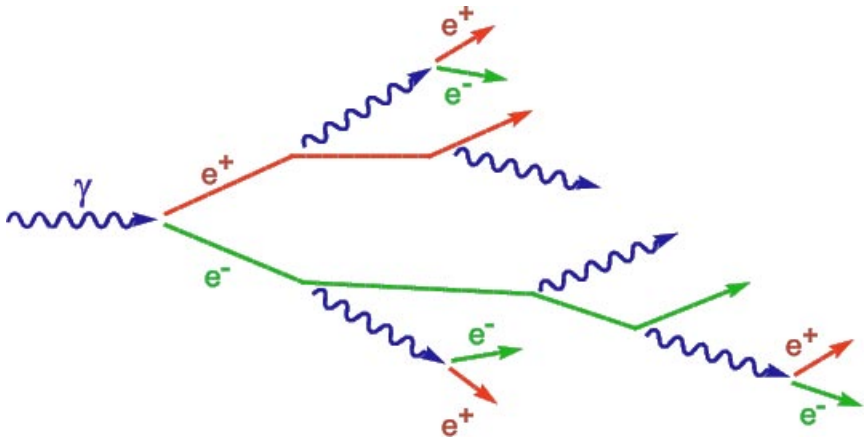

Figure 3.7: Cartoon of an electromagnetic shower.

These showers in turn excite atoms within the crystals; the resultant photons from de-excitation are then detected using silicon photo-diodes. The number of scintillation photons is proportional to the energy deposited by the shower.

The CsI(Tl) crystals are arranged as depicted in Figure 3.8. Tapered trapezoidal CsI(Tl) crystals are arranged in a barrel shape around the detector. The tapered ends are pointed inward slightly off angle from the interaction point to reduce the number of tracks passing through the inactive material between the crystals. Crystal length varies from ~ 16 radiation lengths[6] (X_0) in the backward section to $\sim 17.5X_0$ in the forward section. This reflects the asymmetric nature of the beam and provides cost savings on the expensive CsI(Tl) crystals. Additionally, a forward end cap fully instrumented with $17.5X_0$ crystals adds to polar angle coverage [12].

The EMC is responsible for providing energy, ϕ and θ measurements. Experimentally the resolutions of these measurements were found to be [13]:

$$\frac{\sigma_E}{E} = \frac{(2.30 \pm 0.03 \pm 0.3)\%}{\sqrt[4]{E(GeV)}} \oplus (1.35 \pm 0.08 \pm 0.2)\%$$

[6]The radiation length of a material is the average distance over which an electron loses all but 1/e of its initial energy.

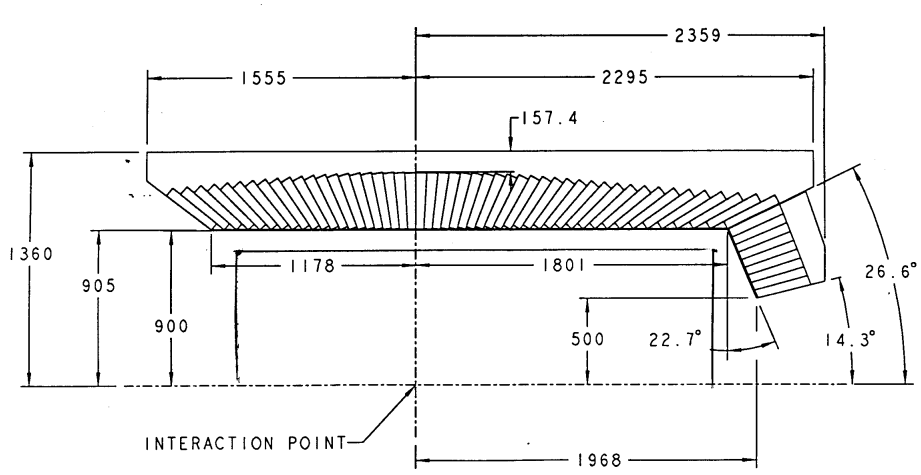

Figure 3.8: Beam-parallel section of EMC crystals [10]

$$\sigma_\theta = \sigma_\phi = \frac{(4.16 \pm 0.04)mrad}{\sqrt{E(GeV}}$$

3.2.5 Instrumented Flux Return

BaBar's outer layer, the Instrumented Flux Return (IFR), is tasked with identification of muons and neutral hadrons. BaBar's magnetic solenoid is enclosed by an iron yolk flux return. This large volume of iron is exploited in the experiment and instrumented to detect outgoing muons and showers produced by neutral hadrons in the iron. Resistive plate chambers (RPC), consisting of parallel resistive bakelite plates separated by gas, are embedded into the iron yolk. Muons are easily able to escape the detector as they are not prone to shower within the material. The RPCs respond quickly to muons ionizing the gas between the plates allowing for a track to be recorded.

Figure 3.9b (left) depicts the RPC design and Figure 3.9b (right) shows the hexagonal

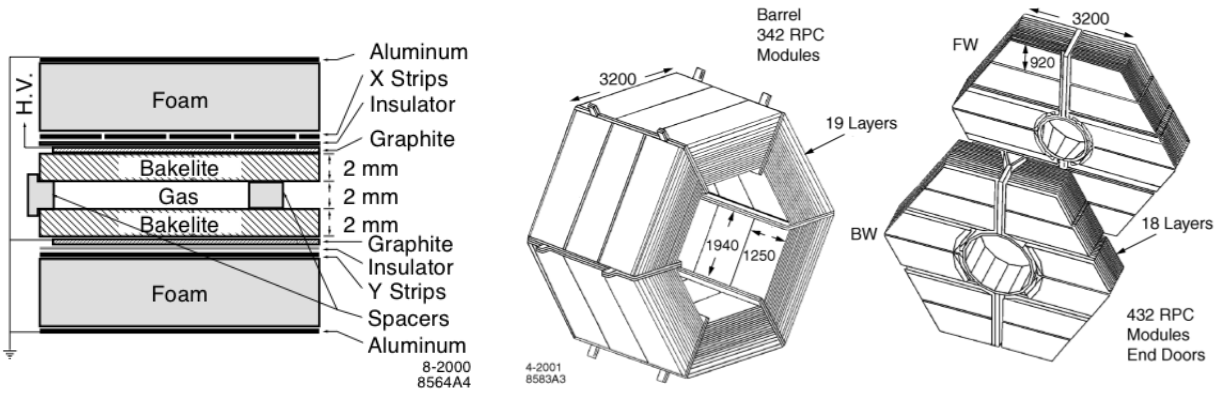

(a) Schematic of a resistive plate chamber (b) Schematic of the IFR geometry

Figure 3.9

design of the IFR. Unfortunately, soon after BaBar began operating, a problem was encountered with the IFR when it was exposed to high temperatures ($\sim 37°C$). Some RPCs began to drop in efficiency and continued to lose efficiency even after a cooling system was added[7]. After careful study of one section of the IFR, it was found that the temperature had caused some of the linseed oil, with which the RPCs were treated, had bunched up and produced 'stalactites', shorting the resistive plates. In 2002, the BaBar barrel IFR was re-instrumented with plastic stream tube detectors[8] to remedy this effect. Roughly half of the data taken makes use of the newly instrumented IFR.

3.2.6 Trigger

Due to the limitations of electronics and storage, the number of collisions occurring within the BaBar detector is much higher than can possibly be recorded. The bunch crossing of 4.2ns corresponds to a rate of 238MHz. The trigger system is responsible for reducing this rate less than $\sim$ 120Hz such that the hardware may handle the incoming data [14].

[7]Some cells dropping as low as 75% muon efficiency

[8]Plastic streamer tubes are gas filled tubs with an anode strung through the centre. Charged particles ionize the gas causing a detectable avalanche.

The trigger system consists of two levels: hardware based 'Level 1' (L1), which reduces the event rate to $\sim$ 1kHz, and software based 'Level 3' (L3) which reduces the rate to $\sim$ 100Hz. 'Level 2' was a planned contingency layer which would have sat between the two.

The L1 trigger relies on information from the DCH, EMC and IFR. Only these components are used as they respond fast enough to fit within the L1 trigger latency window of 12μs [14]. The DCH and EMC provide hit information yielding decision criteria of large transverse momentum and shower size respectively. The IFR provides hit information indicating the presence of muons or neutral hadrons. This information is mainly used for elimination of cosmic backgrounds and for luminosity determination [15].

The L3 trigger makes use of information from the L1 trigger. Implemented in software, the more sophisticated and slower L3 reconstructs all of the events passed to it by L1. A decision is then made on the basis of the topology of the event. Here is where many of the detector background events are removed including Bhabha[9] and beam backgrounds.

[9]Bhabha is the process $e^+e^- \rightarrow e^+e^-$ one of PEP-II's largest backgrounds

Chapter 4

Selection

4.1 Data Set

The *BABAR* data set, collected between 1999 and 2008, is chronologically segmented into 8 runs. Table 4.1 shows the integrated luminosity, nominal beam energy in CM, and number of τ decays associated with each run. The runs consist of 'on-peak' data, which has beam energy (E_B) equal to resonance energy, and 'off-peak' data at a slightly lower energy[1].

This analysis used the TauQED skims [16], a standard subset of the *BABAR* data used for $\mu^+\mu^-$ and $\tau^+\tau^-$ physics studies. Each event is required to pass the L3 trigger and a standard set of background filters[2] (BGF). Charged tracks[3] in the skim are required to satisfy the 'GoodTracksVeryLoose' criteria shown in table 4.2. Lastly, events are required to have fewer than 10 charged tracks and fewer than 12 neutrals[4] with $E > 50\,\mathrm{MeV}$.

[1] Runs 1-6 had on-peak:$E_B = \Upsilon(4S) = 10.58\,\mathrm{GeV}$ and off-peak:$E_B = 10.54\,\mathrm{GeV}$

[2] Algorithms to remove large backgrounds such as Bhabha and beam-beam interactions

[3] Charged particles whose trajectory is reconstructed in DCH and SVT

[4] photons and neutral hadronics reconstructed in the EMC that are not associated with a charged particle

Run	Nominal CM Beam Energy (GeV)	Data $\mathcal{L}$ (fb^{-1}) (on-peak)	(off-peak)	# τ decays (million)
1	10.58	20.547	2.634	42.607
2	10.58	61.003	6.895	124.797
3	10.58	32.063	2.455	63.444
4	10.58	100.214	10.121	202.796
5	10.58	133.091	14.491	271.256
6	10.58	78.554	7.883	158.871
7	10.36	27.963	2.623	64.554
8	10.02	13.599	1.419	35.038
Total				963.363

Table 4.1: Data run characteristics.

'GoodTracksVeryLoose'		'GoodTracksLoose'	
Min p_t	0.0 GeV	Min p_t	0.1 GeV
Max p_t	10 GeV	Max p_t	10 GeV
Min DCH Hits	0	Min DCH Hits	12
Max $DOCA_{XY}$	1.5cm	Max $DOCA_{XY}$	1.5cm
Min $DOCA_Z$	-10cm	Min $DOCA_Z$	-10cm
Max $DOCA_Z$	10cm	Max $DOCA_Z$	10cm

$\mathbf{p_t}$	track transverse momentum
$\mathbf{DOCA_{XY}}$	shortest distance in X-Y plane between track and z-axis
$\mathbf{DOCA_Z}$	shortest distance along z-axis between track and interaction point

Table 4.2: Requirements for 'GoodTracksVeryLoose' and 'GoodTracksLoose' lists.

	Events in millions								Events in thousands
RUN	e^+e^-	$\mu^+\mu^-$	$\tau^+\tau^-$		uds	$c\overline{c}$	B^+B^-	$B^0\overline{B}^0$	$\tau^\pm \to e^\pm\,\gamma$
1	22.8	25.5	20.4	2.0	47.2	58.9	37.0	37.2	108.0
2	62.6	69.5	55.5	7.4	130.9	168.8	103.1	103.4	312.0
3	32.1	37.2	28.0	2.7	66.9	84.0	49.8	50.6	166.0
4	101.3	117.2	90.0	9.2	213. 4	252.8	168.0	167.3	504.0
5	151.8	172.5	132.2	13.3	317.8	366.8	244.2	244.8	666.0
6	41.0	93.2	68.1	5.3	84.4	104.8	68.0	68.1	488.0
7	283.9	68.7	47.6	0.0	111.6	135.2	0.0	0.0	68.0
8	72.5	16.7	12.9	0.0	30.3	37.7	0.0	0.0	30.0

Table 4.3: The total number of MC background events generated (quoted in millions) and MC signal events (quoted in thousands).

4.2 Monte Carlo Simulated Events

In order to properly understand the detector response to signal and backgrounds, it is necessary to produce simulated physics events. These events mimic the output of the detector and are run through the same reconstruction process as the actual data. A Monte Carlo (MC) based simulation software, GEANT4 [17], is run with a full geometrical description of the *BABAR* detector [18] to produce the simulated events. From such simulations, estimates of the efficiency with which signal and background processes are selected can be obtained.

MC events are required for the $\tau^{\pm} \to e^{\pm}\ \gamma$ (signal) and major backgrounds including: generic $\tau^+\tau^-$ decays, $e^+e^- \to e^+e^-$ (Bhabha), $e^+e^- \to \mu^+\mu^-$ (dimuon), $e^+e^- \to (u\bar{u}, d\bar{d}, s\bar{s}\ mixture)$, $e^+e^- \to c\bar{c}$ and $e^+e^- \to b\bar{b}$. Table 4.3 shows the number of events generated by run. For generated events, the run designation signifies that they were generated under the same conditions as the corresponding data run. Events involving two-fermion final states ($\tau^+\tau^-$, Bhabha, dimuon) are generated using the KK2F [19] software package. The TAUOLA [20] package models all tau decays – $\tau^+\tau^-$background and signal events. The remaining $e^+e^- \to q\bar{q}$ processes are modeled using PYTHIA [21] and EVTGEN [22].

To properly compare the MC background events to data, it is necessary to have the same number of data and equivalent MC events. However, production of MC events takes a significant amount of computing power and producing enough MC to match the data , ignoring Bhabha events, is a challenge. Including Bhabha events would be prohibitively expensive since the cross section is roughly 30 times that of the next largest background as shown in table 3.1.

The MC data is scaled to match the data. Despite this, a large MC sample is still necessary. If the sample is too small, scaling will over-emphasize small-scale statistical fluctuations. The weight for the i^{th} type of MC, ω_i, is given as:

$$\omega_i = \frac{N_i^{data}}{N_i^{MC}} = \frac{\sigma_i}{N_i^{MC}} \int \mathcal{L} dt$$

$\mathbf{N_i^{data}}$	number of i^{th} background in data
$\mathbf{N_i^{MC}}$	number of generated i^{th}MC background
$\sigma_\mathbf{i}$	cross-section for producing i^{th} MC background
$\int \mathcal{L}\mathbf{dt}$	integrated luminosity

Table 4.4 shows the scaling factor for each MC type averaged over all runs. The number of Bhabha events generated is far too low, hence it is the only background that must be scaled up.

MC Type	Average Scale
$\mu^+\mu^-$	1.00
$\tau^+\tau^-$	0.75
uds	0.73
$c\bar{c}$	0.51
$b\bar{b}$	0.52
B^0	0.52
e^+e^-	21.22

Table 4.4: Average scaling factor for each MC background type.

4.3 Preselection

To search for a rare decay it is necessary to choose some defining characteristics that will separate it from the multitude of other processes present within the detector. The analysis begins with a loose set of requirements known as 'Preselection' which consists of:

1. An event topology requirement which demands minimum charged track quality and specific geometry

2. The choice of 'signal variables' m_{EC} and ΔE to identify the signal and a requirement on the neutral hits (γ's)

3. The choice of a search region in m_{EC} vs ΔE

4. Loose requirements on signal particle identification

4.3.1 Topology

This analysis studies τ-pair events from the TauQED skims. In the centre of mass (CM) frame the τ's are created back-to-back. Hence, each event may be segmented into two sides – splitting at the interaction point perpendicular to the τ momentum axis. Figure 4.1 shows the sides; the 'signal side' with the interaction $\tau^{\pm} \to e^{\pm}\,\gamma$ and the 'tag side' with a Standard Model decay.

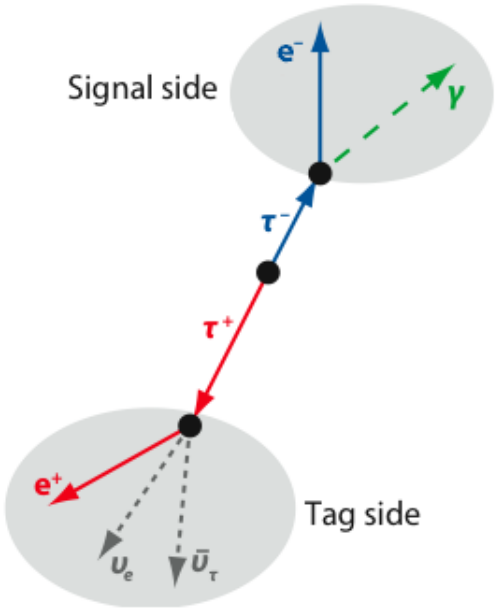

Figure 4.1: Diagram depicting an example τ-pair event split into signal ($\tau^- \to e^-\gamma$) and tag ($\tau^+ \to e^+\nu_e\bar{\nu_\tau}$) in the centre-of-mass frame.

The following track and topology requirements are applied:

- Tracks satisfy the 'GoodTracksLoose' requirement as in table 4.2.

- No track may overlap with tracks resulting from photon conversions ($\gamma \to e^+e^-$) to avoid errors in track reconstruction.

- Events considered must have the '1N' topology with 1 track on the signal side and $N = 1, 3$ tracks on the tag side.

4.3.2 Signal Variables

The Standard Model decay $\tau^\pm \to e^\pm \nu\bar{\nu}$ with initial or final state radiation[5] appears very similar to $\tau^\pm \to e^\pm\ \gamma$ in the *BABAR* detector since the neutrinos are inferred, not detected. Setting these two processes apart is the 'missing' energy that the neutrinos carry away. Define the variable:

$$\Delta E = (E_\gamma + E_{e^\pm}) - E_B$$

$\mathbf{E}_\gamma$	signal photon energy
$\mathbf{E}_{\mathbf{e}^\pm}$	signal electron energy
$\mathbf{E}_\mathbf{B}$	beam energy

Note that for the neutrino-less decay $\Delta E \sim 0$ and for the standard tau decay $\Delta E = E_\nu + E_{\bar{\nu}}$. Hence ΔE may be used to separate these two processes.

Additionally, should a τ decay to e, γ , it is expected that the invariant mass (m_{inv}) of the e, γ system[6] to coincide with the τ mass. A signal-like e, γ system resulting from a background, such as Bhabha with initial state radiation[7], could also coincide with the τ mass, but it is much less likely due to a larger phase space available for such backgrounds. Hence m_{inv} is a useful quantity in identifying $\tau^\pm \to e^\pm\ \gamma$.

Figures 4.2a and 4.2b respectively show the ΔE and m_{inv} distributions for simulated signal events. m_{inv} and ΔE are intuitive choices for the signal identifying variables for the analysis; unfortunately, they are highly correlated for MC signal events. In addition, it is

[5] A photon radiated by the one of the initial electrons or final electrons.
[6] $m_{inv} = E^2 - p^2 = (E_\gamma + E_e)^2 - (\vec{p}_\gamma + \vec{p}_e)^2$
[7] Incoming electron interacts in the beam pipe releasing a photon before collision.

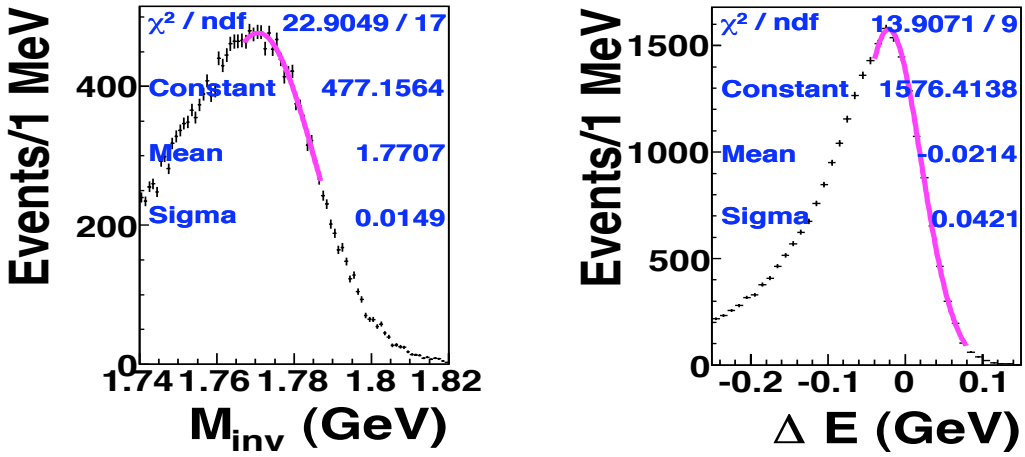

(a) Invariant mass for signal MC.

(b) ΔE for signal MC.

Figure 4.2

possible to vastly improve upon the mass resolution[8] by choosing another variable which is closely related to m_{inv}. An 'energy constrained mass' (m_{EC}) is determined by performing a kinematic fit on the momentum of the e, γ while constraining the energy to the beam energy. The fit is performed on the signal e and all γ candidates which lie within the EMC[9] acceptance and have an energy over 200 MeV. If a fit is successful then best fit is chosen as the signal photon, otherwise the event is discarded.

Replacing m_{inv} with m_{EC} improves the resolution by over 3 MeV (21%). Figure 4.3a shows the m_{EC} distribution. The derivation of m_{EC} and its advantages over m_{inv} are detailed in Appendix A.

One further improvement can be made to the mass variable. m_{EC} is a function of the angle between the signal photon and electron:

[8] Standard deviation (sigma) of the m_{inv} distribution.

[9] $cos\theta_{LAB} \in [-0.76, 0.92]$

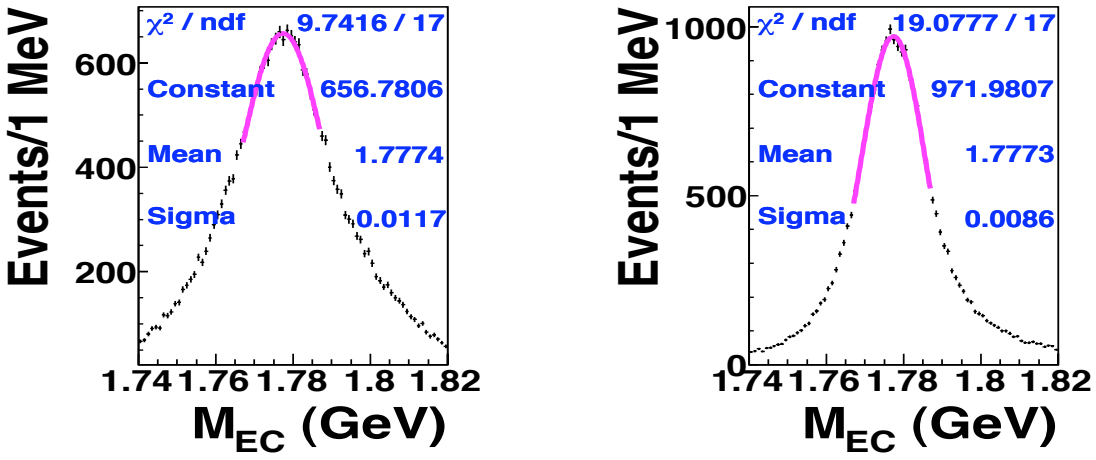

(a) Energy constrained mass without vertex correction.

(b) Energy constrained mass with vertex correction.

Figure 4.3

$$m_{\mathrm{EC}} = g(\vec{p_\gamma} \cdot \vec{p_e}) = f(cos\alpha)$$

$\tilde{\mathbf{p}_\gamma}$	signal photon momentum
$\tilde{\mathbf{p}_\mathbf{e}}$	signal electron momentum
α	angle between signal photon and electron

While the trajectory of the electron is well known[10], the trajectory of the photon must be reconstructed with only information from the EMC. This results in a large uncertainty in the trajectory since the origin of the photon is not well known. A large uncertainty in the trajectory leads to a worse resolution in $m_{\mathrm{EC}} = f(cos\alpha)$. With the reasonable assumption that the origin of the photon is the point of closest approach to the signal electron, the uncertainty in the trajectory drops giving an m_{EC} as in Figure 4.3b. This gives a further 3 MeV (27%) improvement in the resolution.

[10]Charged track is measured in the SVT, DCH and stopped in EMC

The majority of the MC signal events lie within 2σ of the central value of $m_{\rm EC}$ and ΔE. This 2σ ellipse is known as the 'signal region'.

4.3.3 Search Region

In order to efficiently search the *BABAR* dataset for a rare decay such as $\tau^{\pm} \to e^{\pm}\,\gamma$, it is necessary to focus the analysis on a sample of interest. The characteristics of the simulated signal events are used to define such a sample.

Ideally, one could use the 'signal region', defined in section 4.3.2, for a search region. Unfortunately events that appear very similar to $\tau^{\pm} \to e^{\pm}\,\gamma$, such as $e^+e^-\gamma \to e^+e^-\gamma$, also lie within the signal region potentially swamping the small signal. To reduce such background processes it is necessary to analyze the data set in variables other than $m_{\rm EC}$ and ΔE, such as p^{CM}_{trk}[11], so that backgrounds may be identified and removed. In order for this process to be effective in separating the signal from background, it is necessary to consider a wider region of interest for the analysis than just the signal region. Thus the 'grand signal box' (GSB) and 'extended grand signal box' (EGSB) are defined as:

EGSB	**GSB**
$1.25\,\text{GeV} < m_{\rm EC} < 2.25\,\text{GeV}$	$1.50\,\text{GeV} < m_{\rm EC} < 2.1\,\text{GeV}$
$-1.1\,\text{GeV} < \Delta E < 0.6\,\text{GeV}$	$-1.0\,\text{GeV} < \Delta E < 0.5\,\text{GeV}$

These two regions are used as consecutive refinements to the selection process. Figure 4.4 (top) shows the regions associated with this analysis. The 'blinded region' will be discussed in the next section. Figure 4.4 (bottom) shows the distribution of signal, MC background and data in $m_{\rm EC}$ vs ΔE.

[11] signal momentum in CM

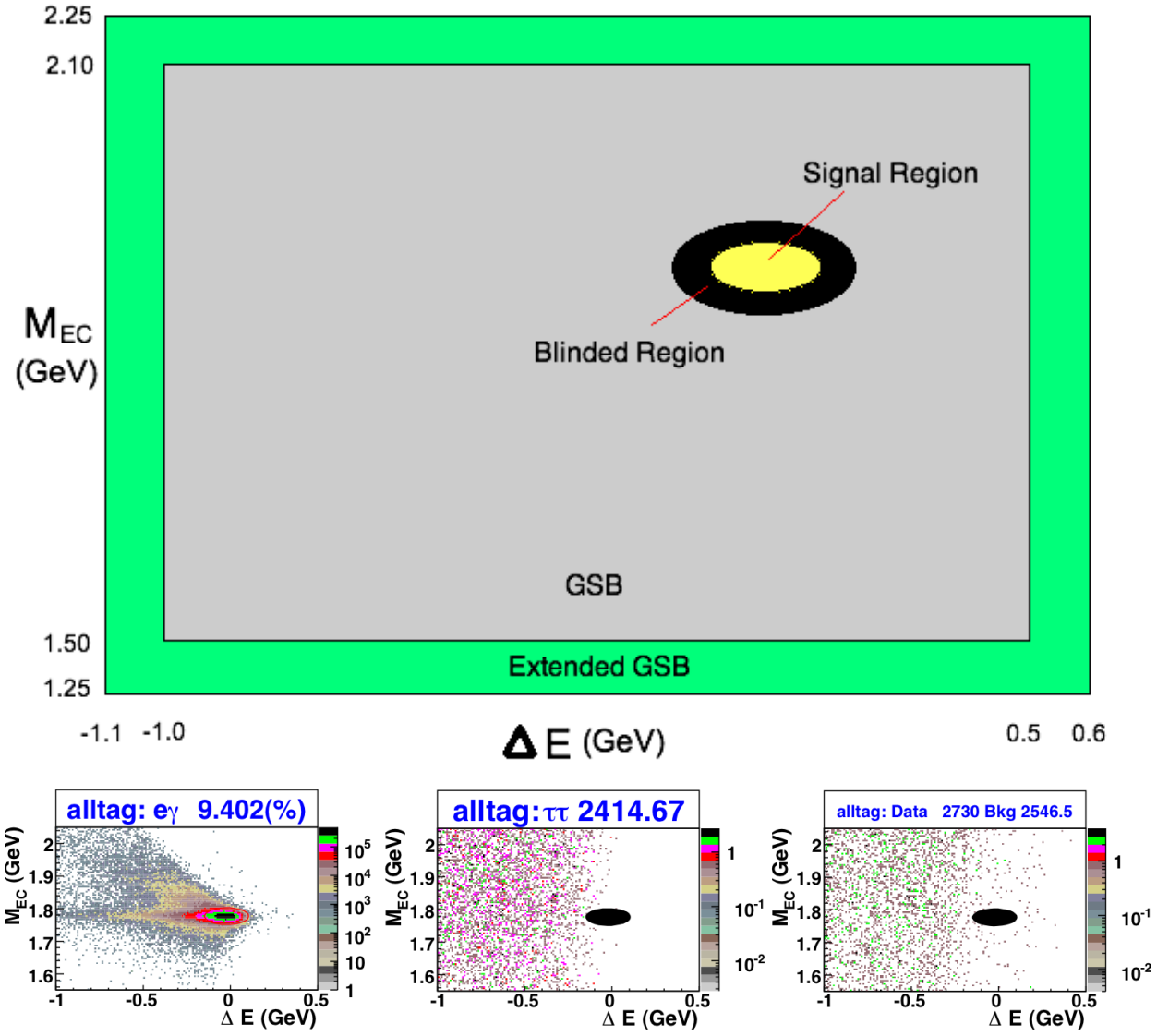

Figure 4.4: Top: Diagram showing the 4 regions in $m_{\rm EC}$ and ΔE: EGSB, GSB, Blinded and Signal regions.

Bottom: $m_{\rm EC}$ vs ΔE for signal (left) MC background (middle) and data (right). The blacked out area is the blinded region.

4.3.4 Particle Identification

BABAR has a standard set of criteria for particle identification (PID). Each 'pid selector' takes event characteristics as input and returns a binary yes/no output. The selectors come in various strengths ("loose", "veryloose", "tight") indicating the certainty of an identification. The "loose" PID will select more background and have a higher efficiency than the "tight" PID. These selectors are set as flags on each track to be used during analysis. Loose requirements are applied to the signal tracks in this analysis such that 98.9% (see table 4.5)[12] of MC signal events within the EGSB are accepted. This selection, known as 'Loose Lepton Tag', requires each signal track pass one of the following selectors:

eMicroVeryLoose	muBDTVeryLoose
eKMsuperLoose	muBDTVeryLooseFakeRate
muNNVeryLoose	muBDTLoPLoose
muNNVeryLooseFakeRate	

e	electron selector
mu	muon selector
Micro	selector decides based on hard requirements on event variables
BDT	selector decides based on a boosted decision tree algorithm
NN	selector decides using a neural net
KM	selector based on combination of hard requirements and neural net
FakeRate	minimize fake identification

4.3.5 Summary

Table 4.5 shows the effect of each preselection requirements on the data and each type of MC. Signal MC is quoted as an efficiency. Once preselection is complete, the MC signal efficiency is reduced to 36.09%.

[12]Signal efficiency in Table 4.5 before and after lepton tagging (Loose LepTag) are 36.49% and 36.09% respectively giving a 98.9% PID efficiency

Selection Requirement	Data Events	e^+e^- Events	$\mu^+\mu^-$ Events	$\tau^+\tau^-$ Events	uds Events	$c\bar{c}$ Events	$b\bar{b}$ Events	Sig Eff (%) $\tau^\pm \to e^\pm\,\gamma$
L3 Trigger	2328.8	53.7	9004.3	285.1	252.3	127.1	91.05	90.3
Background Filters	1976.9	8.0	8985.9	276.8	248.4	126.3	73.36	65.6
TauQED Skim	1639.8	7.6	8973.1	274.9	185.0	92.2	69.11	61.5
11 & 1N Topology	1043.7	5.3	8586.5	234.9	54.2	23.8	60.11	52.4
$m_{\rm EC} fit(E_\gamma > 0.2\,{\rm GeV})$	341.1	2.9	751.3	144.3	45.7	20.6	53.62	47.4
Loose GSB	15.9	0.2	215.9	0.8	1.6	0.10	44.26	36.5
Loose LepTag	13.2	0.2	199.8	0.3	0.3	0.03	40.95	36.1

Table 4.5: Numbers of events (millions) surviving successive application of the preselection criteria. All runs are added together with MC scaled to data luminosity.

4.4 Selection

The purpose of this analysis is to measure the branching fraction for $\tau^\pm \to e^\pm\,\gamma$. Should there be no evidence for signal, it is desirable to arrive at the lowest upper limit (UL) possible. From equation 2.3, to determine the lowest possible upper limit, the signal efficiency, ϵ, should be preserved. In addition, if we take the assumption that no signal exists, the term $N_{signal}^{90\%CL}$ decreases quickly with the number of selected backgrounds. Hence, it is beneficial to carry out the selection process with mind to preserve efficiency and reduce backgrounds.

The selection process is carried out by examining the data, background and signal characteristics that help discriminate background from signal. With that information, a 'selection requirement' is placed on that event characteristic (variable) at first by eye. Events which do not satisfy this selection requirement are discarded from the analysis. Several variables are scrutinized and ten selection requirements are made.

An expected UL is calculated using the MC background distribution within the signal region as an estimate for the number of data events in the signal region. All the selection requirements are now shifted a small amount and the UL is re-calculated. Should any shift cause a drop in the UL, the selection requirement is changed by that

shift, and the entire analysis is re-run. This process is repeated until it arrives at a stable, lowest upper limit.

A possible danger in this optimization process is that the experimenter could discard signal events in a manner that inadvertently biases the result. The experimenter is able to introduce a bias by tuning the selection criteria based on the final result (branching ratio, or upper limit on branching ratio). This bias can be overcome by hiding data that lies within 3σ region in $m_{\rm EC}$ and ΔE centreed on their central values. This region is known as the 'blinded region' as shown in Figure 4.4.

The rest of the analysis is now carried out without knowledge of the data in the signal region. All selection requirements are made based on MC samples which contain no signal events. Now it is safe to remove MC backgrounds without introducing bias into the selection process. In addition, the data may be used in the remaining GSB to ensure data/MC agreement.

4.4.1 Particle ID, the GSB and Tagging

At this point a more stringent requirement is placed on the signal track particle ID. e signal tracks must satisfy the 'eLHTight' selector. This restriction is placed after preselection and is determined through the optimization process (discussed in Section 4.5). Also events are required to lie within the GSB as defined in Section 4.3.3.

Before applying selection requirements, it is helpful to partition the analysis by tag-side particle content. For example, the probability that a particular event is a radiative Bhabha ($e^+e^-\gamma \to e^+e^-\gamma$, the dominant background in this study) is far larger if the tag-side charged track is an electron than if it is a muon. The e-tag event may be treated differently from other tags to leverage this information.

Table 2.4 shows the major decay modes that the tag-side τ may undergo. It

is appropriate to partition the tag-side particle content according to these common decays. The leptonic decays ($\tau^- \to e^-\bar{\nu}_e\nu_\tau$, $\tau^- \to \mu^-\bar{\nu}_\mu\nu_\tau$) make up $\sim 35\%$ of all τ decays, hence an electron and muon tag designation is appropriate. Many decays with charged pion products are expected; hence a pion tag designation is applied. Events with charged pions may be partitioned further since the largest decay mode ($\tau^- \to \pi^-\pi^0\nu_\tau$) is nearly consistently a resonant decay ($\tau^- \to \rho^-\nu_\tau \to \pi^-\pi^0\nu_\tau$). Such resonant decays are separated into a ρ-tag. Finally all events with three tag-side charged tracks, such as $\tau^- \to \pi^-\pi^-\pi^+\nu_\tau$, are included as a three-pronged hadronic ($3h$) tag. These tag designations cover the vast majority of tag-side τ decays; thus, the events are classified as follows:

- e-tagged: there is track on the tag side; the track passes 'eMicroVeryLoose' and fails 'muBDTTightFakeRate'; the total neutral energy (CM) on the tag-side is less than 200 MeV[13].

- μ-tagged: there is one track on the tag side; the track passes 'muBDTTight-FakeRate' and fails 'eMicroVeryLoose'; the total neutral energy (CM) on the tag-side is less than 200 MeV.

- π-tagged: there is one track on the tag side; the track fails 'eMicroVeryLoose' and fails 'muBDTTightFakeRate'; the total neutral energy (CM) on the tag-side is less than 200 MeV.

- ρ-tagged: there is one track on the tag side; the track fails 'eMicroVeryLoose' and fails 'muBDTTightFakeRate'; the tag-side contains a π^0 candidate satisfying 'Pi0VeryLoose'.

[13]Cap on tag-side neutral energy reduces mis-identified π^0 events

	$\tau^{\pm} \to e^{\pm}\,\gamma$ Signal Eff(%)			Events in MC Backgrounds			Events in Data		
Tag	GSB	3σ Ell.	2σ Ell.	GSB	3σ Ell.	2σ Ell.	GSB	3σ Ell.	2σ Ell.
e	4.2	2.2	1.6	1161987.4	25454.7	10761.8	1435831	?	?
μ	4.8	2.5	1.8	4355	5.9	2.1	5151	?	?
π	5.8	3	2.2	116258.5	3309.5	1330.1	179506	?	?
ρ	7	3.7	2.7	6700.6	62.2	2.1	8284	?	?
$3h$	3.1	1.6	1.2	4270	7.6	2.6	5709	?	?
all	24.9	12.9	9.6	1293571.6	28839.7	12098.9	1634481	?	?
all but e	20.6	10.7	7.9	131584.3	3385.1	1337	198650	?	?

Table 4.6: Breakdown of events by tag charged track after preselection and PID requirements.

- $3h$-tagged: there are three track on the tag side; all tracks fail 'eMicroVeryLoose' and fail 'muBDTTightFakeRate'; the tag-side contains at most one π^0 candidate satisfying 'Pi0VeryLoose'.

Table 4.6 shows the breakdown of data, MC and signal efficiency by tag-side track in the GSB, blinded and signal regions. Note that the number of MC events does not well match the number of data despite the MC scaling. This is due to the poor modeling of Bhabha events. This problem can be remedied by placing selection requirements to remove Bhabha events.

4.4.2 Variable Requirements

Before beginning variable based selection requirements, attention is required with the data/MC discrepancy arising from poor Bhabha modeling.

Figure 4.5 shows the distribution of the sum of the momenta ($\sum P_{CM}^{Tag}$) of all reconstructed charged and neutral particles on the tag-side for e-tagged events in the GSB. All selection requirements are applied to the plot except the requirement on $\sum P_{CM}^{Tag}$ (indicated by the black arrow) such that the effect of the requirement is clear. Each entry in the Figure 4.5 corresponds to one event. Here the data shown

as black points with error bars; the $\tau\tau$ background shown in red and the Bhabha background shown in blue. The fuchsia line shows the distribution for signal MC and is scaled arbitrarily for convenience.

Ideally, the $\tau\tau$ and Bhabha backgrounds should sum to the number of data events. That is not the case as there are 680 data and 482.2 MC background events (discrepancy of 29%). Due to the insufficient number of Bhabha events, the scaling fails to accurately model the data as can be seen by the poorly modeled peak in the data larger than $\sim 0.8\,\text{GeV}$. This issue can not be rectified for the e-tag. The number of Bhabha events present is too large and the scaling fails due to lack of MC Bhabha statistics. Thus the e-tag sample is not suitable for this search. The e-tag is removed from the search; but, it is not discarded. The e-tagged events are still valuable in identifying Bhabha characteristics to help remove this class of backgrounds from the other tags.

The selection is now carried out on the remaining tags. The main goals of placing requirements are to remove sections of the data dominated by Bhabha events and therefore do not agree well with MC and to increase signal:background (S:B) ratio. It is necessary, however, to preserve as many signal events as possible. The requirements are initially applied by eye and later refined through the optimization process described in chapter 4.5.

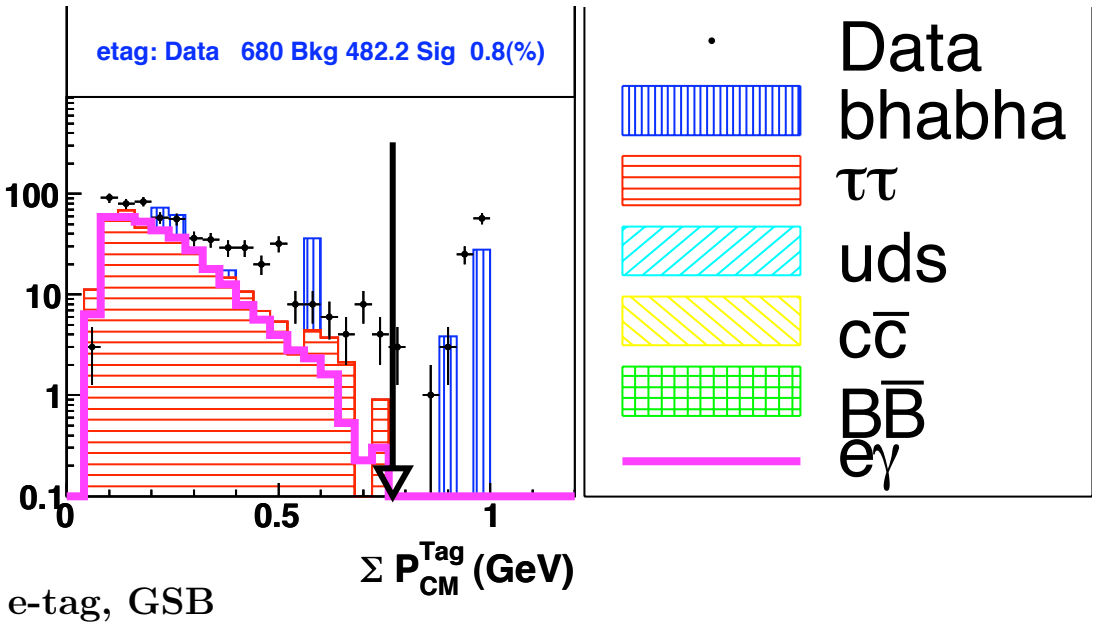

Figure 4.5: Distribution of the sum of the momenta ($\sum P_{CM}^{Tag}$) of all reconstructed charged and neutral particles on the tag-side for e-tagged events in the GSB. All selection criteria are applied to this plot except the requirement on $\sum P_{CM}^{Tag}$.

4.4.3 Selection Requirements

The first six selection requirements are applied to all tags. The final four requirements are tag specific in order to leverage tag characteristics to improve the selection. All plots are shown after application of the neural network selection requirement.

Requirement #1: θ_{miss}

Description	polar angle of missing momentum
Requirement	$\cos(\theta_{miss}) \in [-0.76, 0.92]$
Reason	Necessary to ensure that missing momentum is within the detector acceptance. Hence, the missing momentum corresponds a neutrino and cannot be attributed to a detectable track which exits the detector outside of acceptance

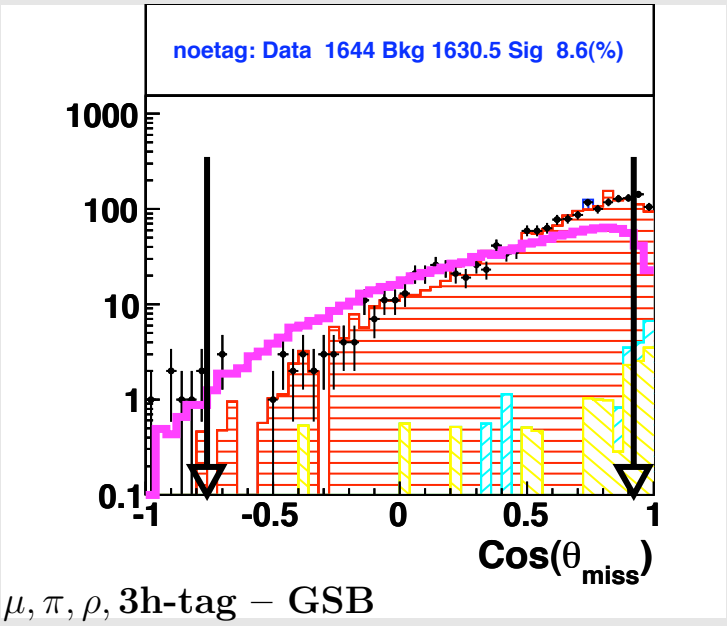

μ, π, ρ, **3h-tag – GSB**

Requirement #2: N^{γ}_{EXTRA}

Description	Number of extra signal side photons with $E > 100\,\mathrm{MeV}$
Requirement	$N^{\gamma}_{EXTRA} = 0$
Reason	Necessary to reduce the misidentification of signal photon. Improves signal:background ratio.

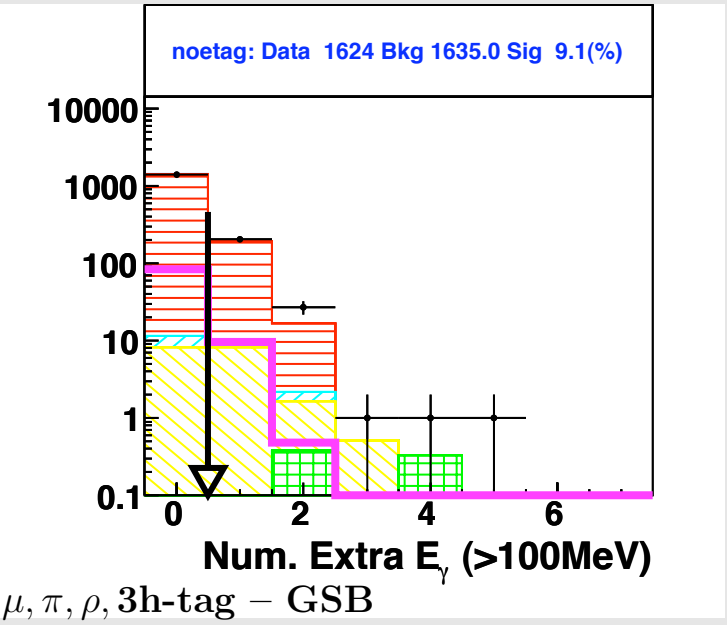

μ, π, ρ, 3h-tag − GSB

Requirement #3: $E_{\gamma}^{CM}, \pi^0_{significance}$

Description	Signal photon energy in CM
	Estimated probability of signal photon being a π^0 daughter
Requirement	$E_{\gamma}^{CM} > 3\,\text{GeV}$ and $\pi^0_{sig} < 0.1$
Reason	To reduce $\tau^{\pm} \to (\pi, K)^{\pm}\, \pi^0\, \nu$ with π^0 energy greater than 3 GeV.

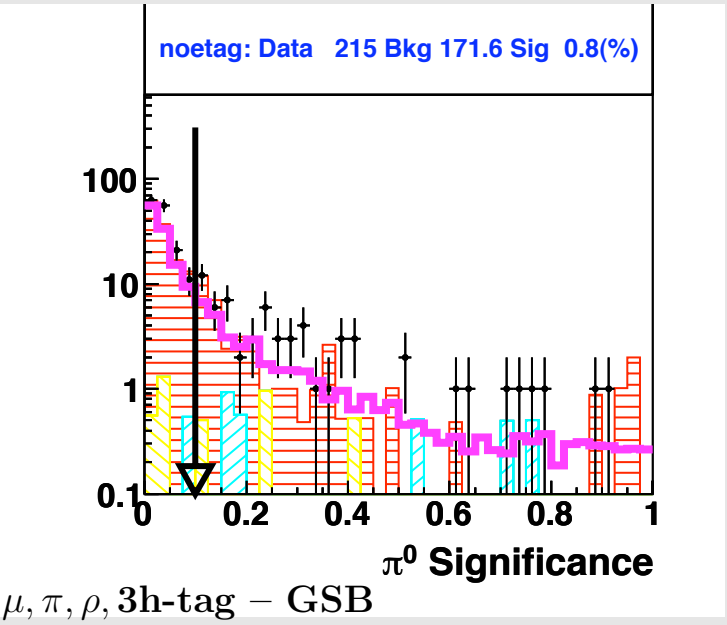

μ, π, ρ, **3h-tag − GSB**

Plot for only events with $E_{\gamma}^{sig} > 3.0\,\text{GeV}$

Requirement #4: $\theta_{\gamma-e}$

Description	Angle between signal photon and signal track in CM
Requirement	$\cos(\theta_{\gamma-e}) < 0.786$
Reason	To remove small angle $\tau^+\tau^-$background events. The opening angle is kinimatically limited for $\tau^\pm \to e^\pm\ \gamma$

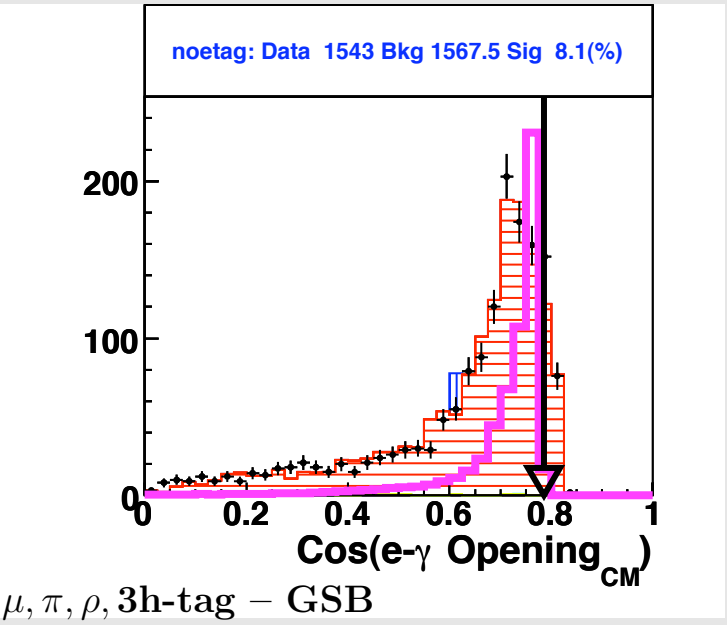

μ, π, ρ, **3h-tag − GSB**

Requirement #5:	E_γ^{CM}
Description	Signal γ energy in CM
Requirement	$E_\gamma^{CM} > 1.0\,\text{GeV}$
Reason	To increase signal:bkg ratio. Low energy γ in $\tau^\pm \to e^\pm\,\gamma$ are improbable due to kinematics; hence, it is possible to remove background without reducing efficiency.

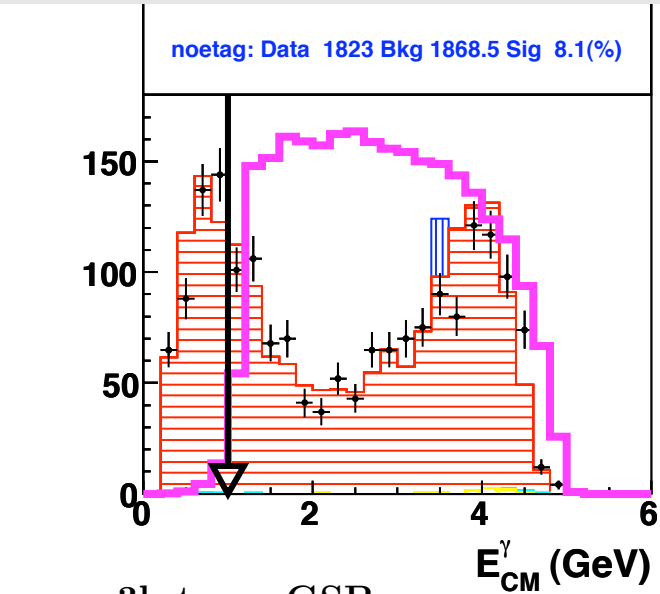

μ, π, ρ, **3h-tag – GSB**

Requirement #6: P_e^{CM}/E_B

Description	Signal track momentum (CM) divided by beam energy
Requirement	$P_e^{CM}/E_B < 0.77$
Reason	To remove Bhabha background events which have e with energy close to beam energy.

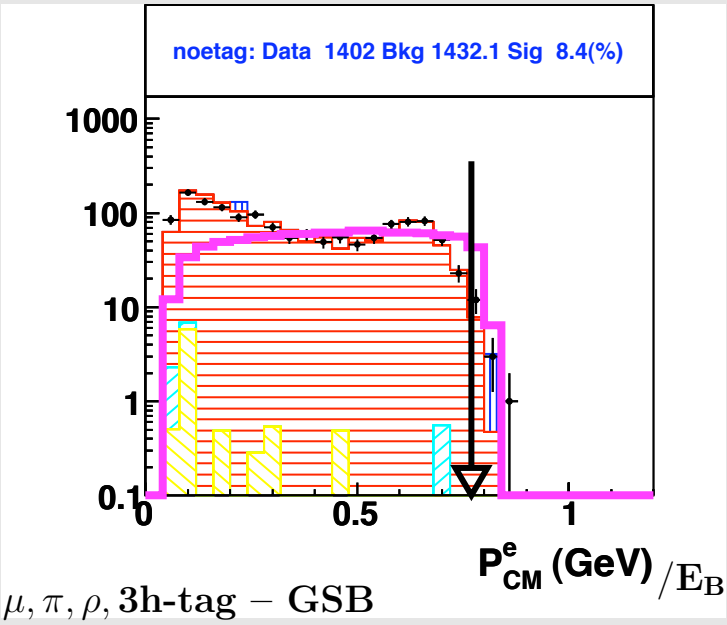

μ, π, ρ, **3h-tag − GSB**

Requirement #7:	$\sum P_{tag}^{CM}/E_B$
Description	Total tag-side momentum (CM) divided by beam energy
μ, π-tag	$\sum P_{tag}^{CM}/E_B < 0.77$
ρ, **3h**-tag	$\sum P_{tag}^{CM}/E_B < 0.90$
Reason	To remove Bhabha background events which have high tag-side momentum.

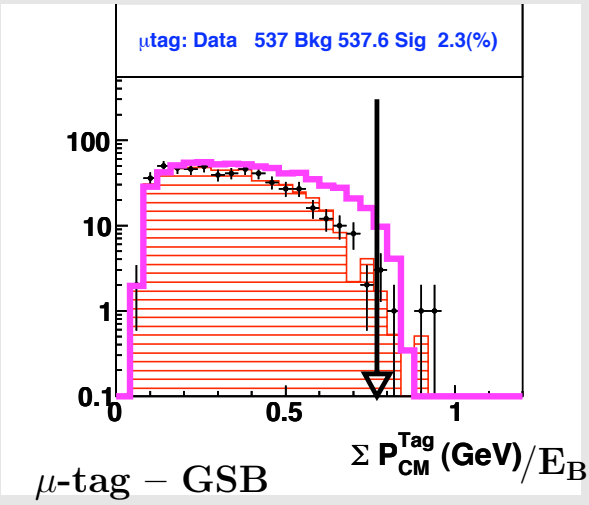

μ-tag – GSB

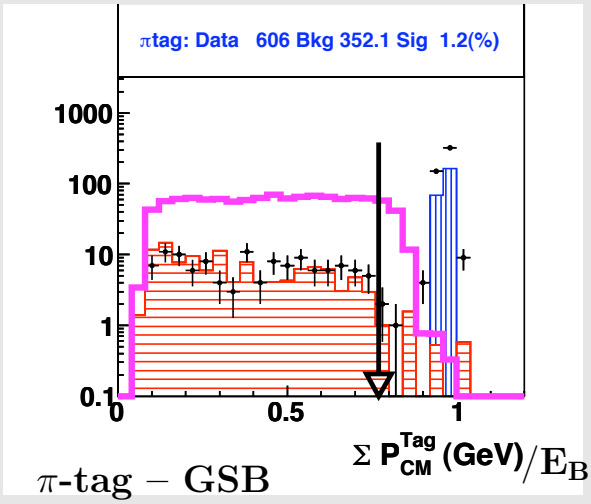

π-tag – GSB

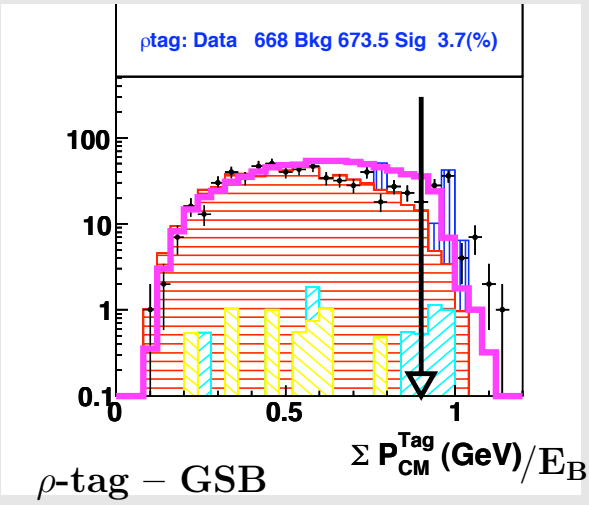

ρ-tag – GSB

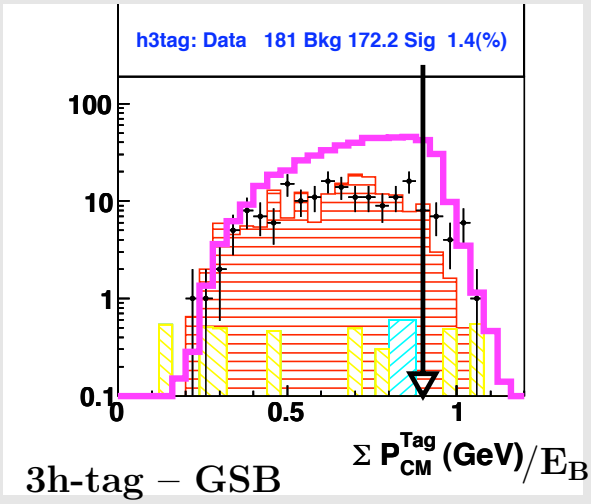

3h-tag – GSB

Requirement #8:	M_{tag}^{pseudo}
Description	Tag side reconstructed invariant mass assuming that the τ neutrino is massless and co-linear with the charged track system
μ, π-tag	$M_{tag}^{pseudo} < 0.5\,\text{GeV}$
$\rho, 3h$-tag	$M_{tag}^{pseudo} < 1.777\,\text{GeV}$
Reason	See appendix B

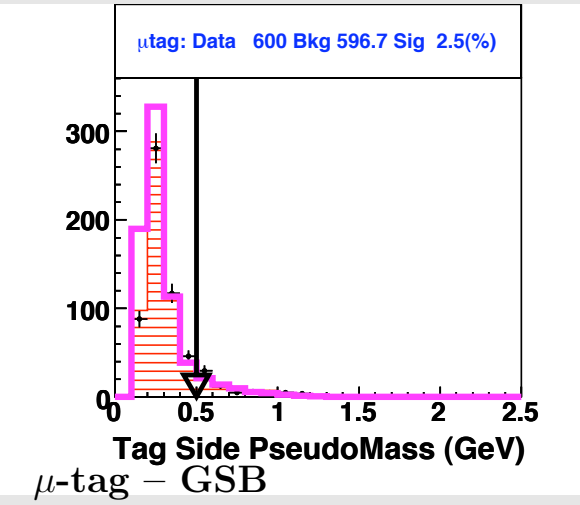

μ-tag – GSB

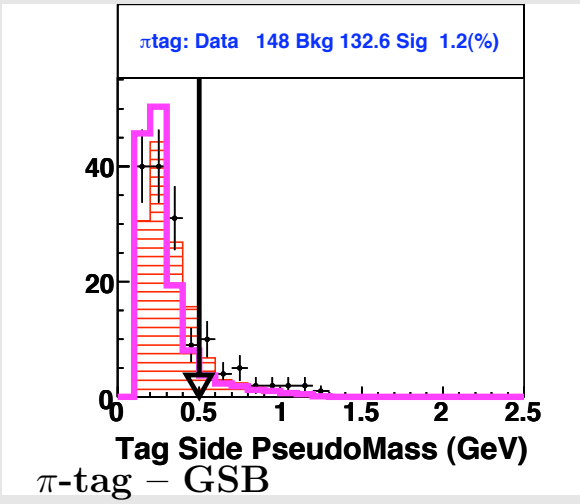

π-tag – GSB

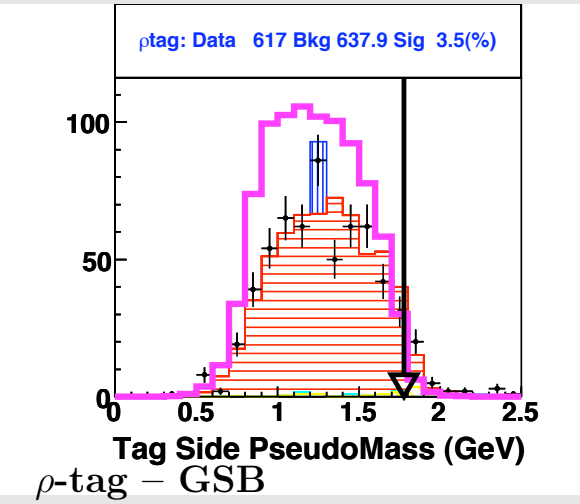

ρ-tag – GSB

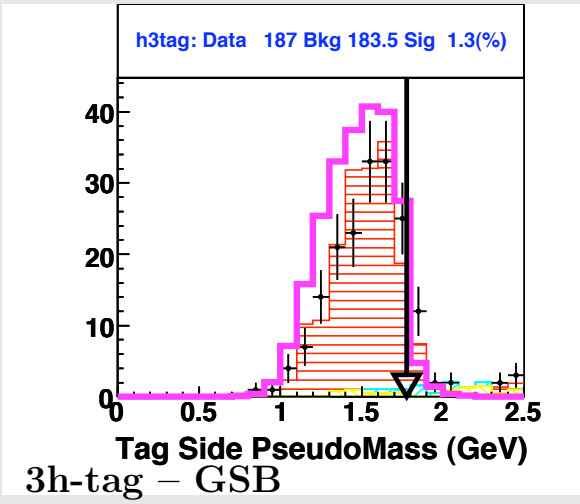

3h-tag – GSB

Requirement #9:	M_ν^2
Description	Inferred mass squared of neutrino on tag-side.
μ-tag	$M_\nu^2 > -0.25$
$\pi, 3h$-tag	$\lvert M_\nu^2\rvert < 0.25$
ρ-tag	$\lvert M_\nu^2\rvert < 0.5$
Reason	In π-tag the signal distribution is spiked at zero as there is only one τ neutrino. Bhabha, which lacks a neutrino, shows a non-zero neutrino mass; hence, M_ν^2 can be used to remove Bhabhas from the data. $3h$-tag peaks at zero as there is only one neutrino present; selecting on M_ν^2 allows an improvement in S:N. μ-tag signal gives a positive M_ν^2 due to the presence of two neutrinos; it is also useful in reducing S:N because the primary background $\tau \to \mu\bar{\nu}_\mu\nu_\tau$ doesn't peak due to the two neutrinos.

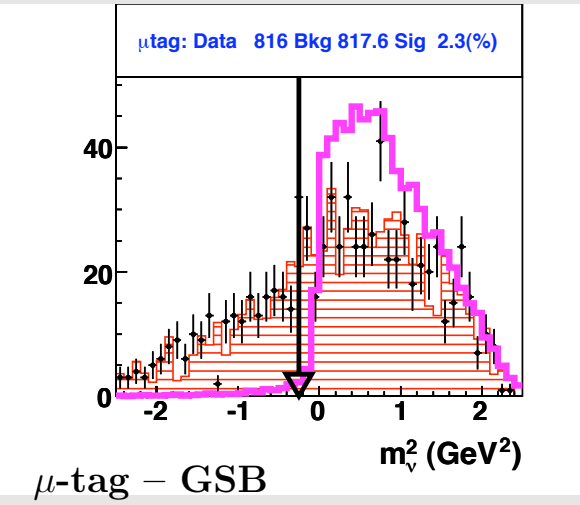

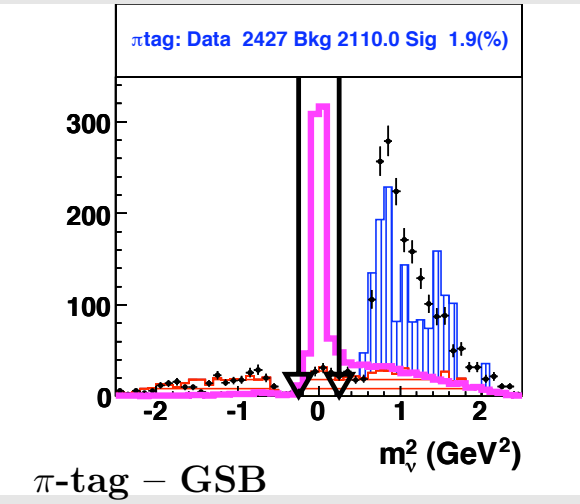

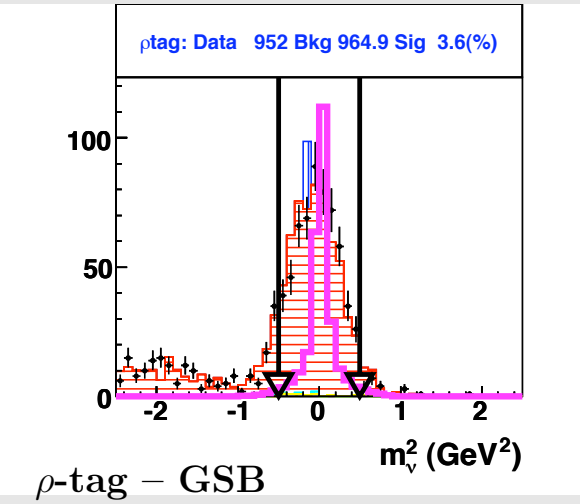

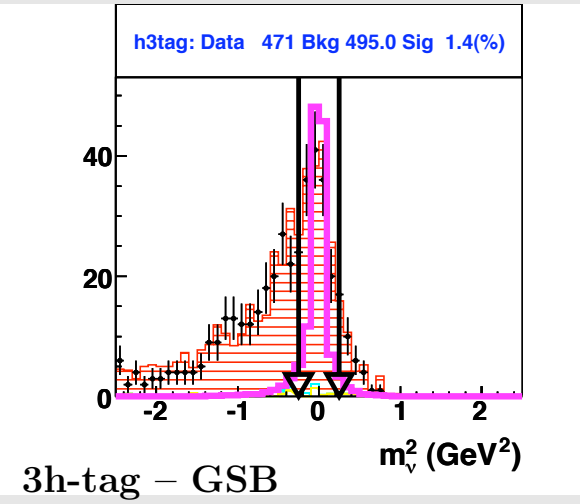

Requirement #10: p^T_{miss}, E_B

Description	Missing transverse momentum, beam energy
μ, π-tag	$-ln(\lvert p^T_{miss}\rvert / E_B) < 2.0$
$\rho, 3h$-tag	$-ln(\lvert p^T_{miss}\rvert / E_B) < 4.0$
Reason	To $\tau\tau$ remove backgrounds as $\tau^{\pm} \rightarrow e^{\pm}\ \gamma$ has low p^T_{miss} due to lack of neutrinos.

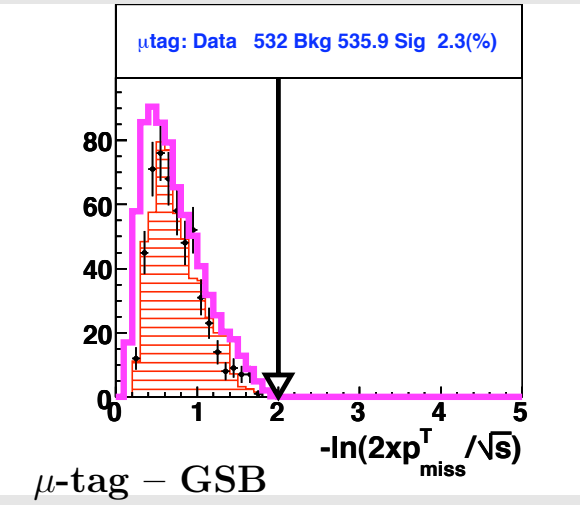

μ-tag – GSB

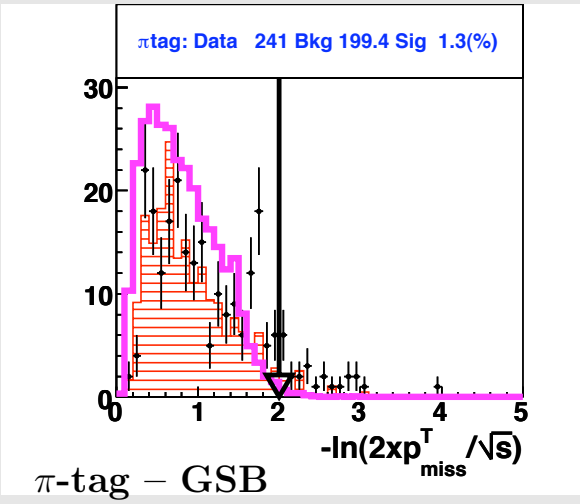

π-tag – GSB

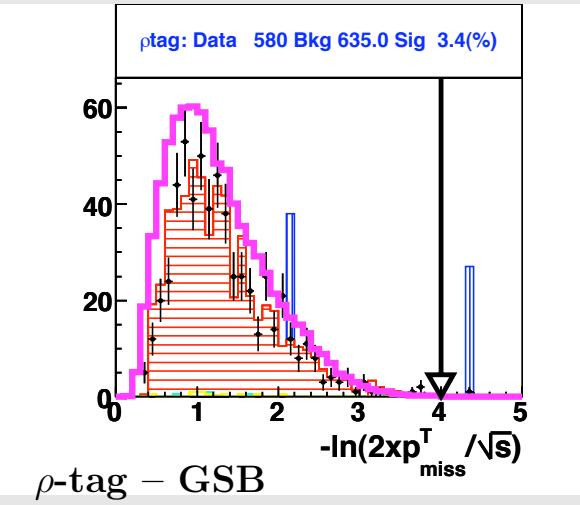

ρ-tag – GSB

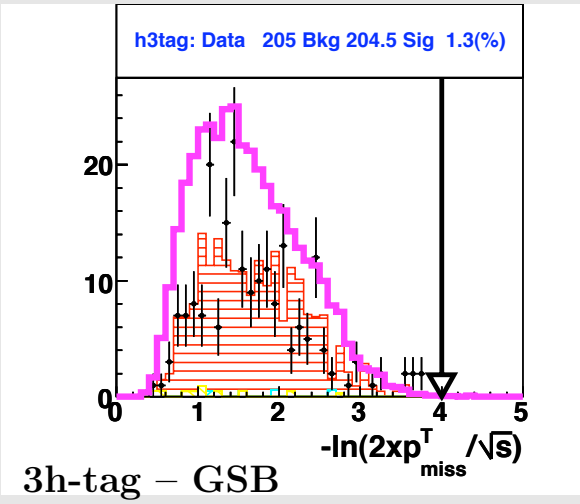

3h-tag – GSB

4.4.4 Neural Net Requirement

It may occur that signal and background are inseparable in one dimension, but are quite easy separated in more than one. Many combinations of variables must be considered (linear or otherwise) relying on the human eye or intuition to determine correlations. Two methods were considered for multi-dimensional requirements: the Fisher method and artificial neural networks (NN).

The Fisher method [23] is a statistical method which involves constructing a linear combination of input variables to act as a discriminant. The signal and background MC are used to construct the discriminant such that the separation between the two distributions is maximal.

Artificial neural networks are a set of nodes (neurons) and weighted connections (synapses) which act as a function that discriminates between signal and background. An example structure is shown in Figure 4.6a. The neurons are in blue and the synapses in black. The thickness of the synapse line represents the weighted factor associated with that connection. The first layer of neurons are fed the six event characteristics. These neurons then normalize the input, multiply it by a weight and pass the value onto the next set of neurons. The inner set of neurons takes weighted inputs from each of the neurons in the previous layer, computes a linear combination of the inputs and outputs a weighted value to each of the neurons in the next layer. The final set of neurons passes their weighted values to the output neuron where a linear combination is formed and returned.

The network is constructed by 'training' it based on signal/background event characteristics. Training involves passing the data set through the network multiple times. After each pass, the network evaluates a cost function (separating signal and background distributions) and rearranges its geometry to converge on a good discrim-

inating algorithm. The advantage of the neural network over a Fisher discriminant is it is able to pick up non-linear relationships between the variables. The final analysis makes use of a neural network, but not a Fisher discriminant. Many combinations of variables were investigated for both techniques and it was found that the neural net provided sufficient discrimination while requiring few variables.

The ROOT implementation of the multilayer perceptron [24] type neural network is employed in the selection process. Figure 4.6a shows an example neural net geometry. The six input variables are defined in Appendix C and plotted in Figure C.2. Candidates for NN variables may have distributions in which signal and background differ greatly (M_ν^2) allowing for discrimination. Other variables (P_t^{miss}) are included because of known helpful discriminating power when combined into multi-dimensional requirements.

Figure 4.7 shows the output of the neural network for each tag. The neural network is especially useful for improving S:B ratio in the μ and $3h$ tags.

4.4.5 Selection Summary

Table 4.7 shows the progression of the data set through the event selection process. Once the single variable requirements are applied, the $b\bar{b}$ sample is completely removed. There are 1389 data and 1423 MC background events in the GSB ($2.4 \pm 0.1\%$ disagreement). Table 4.7 shows after completion of the selection requirements an efficiency of 3.9% remains in the signal region.

4.5 Optimization

The first sweep of event selection involves making selection requirements by eye. Refinement of these requirement values are made through a process known as opti-

Selection Requirement	Data Events	MCtot Events	$\tau^+\tau^-$ Events	*uds* Events	cc Events	e^+e^- Events	Margin Eff (%)	Cumul Eff (%)
1. PID Selector	433645	283880	43525	1333	2381	236430	21.40	21.4
2. GSB requirement	198650	128199	18317	519	1020	108254	96.4	20.6
3. Single Variable Reqs	2138	2096	2054	3.93	12.43	26.25	41.8	8.6
4. Neural Net Requirement	1389	1423	1385	3.41	8.16	26.25	93.7	8.1
5. Blinded Box	Blinded	2.44	2.44	0.00	0.00	0.00	87.1	5.2
6. Signal Box	Blinded	0.00	0.00	0.00	0.00	0.00	75.9	3.9

Table 4.7: Result of successive application of selection criteria.

mization. Here a prediction of the upper limit (UL) on the $\tau^{\pm} \rightarrow e^{\pm}\ \gamma$ branching fraction is made (under the assumption there is no signal), variable requirements are varied slightly and the selection/optimization process is repeated until a minimal, stable upper limit is achieved.

4.5.1 Upper Limit Prediction

To predict the UL on the branching ratio, a prediction of the number of background events inside the signal region is made. To do this a background PDF[14] is fit to the unblinded MC events in the GSB using a binned maximum likelihood method. The background PDF is derived from the MC background within the signal region.

After selection, the two remaining substantial background distributions are Bhabha and $\tau\tau$. The *uds* and $c\bar{c}$ distributions are quite negligible (table 4.7) and are simply added to the $\tau\tau$ distribution to simplify the fit. The Bhabha MC sample is insufficient for the fit, it is too granular. Instead a sample of Bhabhas is taken from the unused e-tag data. Hence the background PDF is:

$$PDF_{bkg} = (f_{e^+e^-} \times PDF^{DATA}_{e^+e^-}) + ([1 - f_{e^+e^-}] \times PDF^{MC}_{\tau\tau})$$

Here $f_{e^+e^-}$ is determined by fitting the Bhabha distribution to the data outside

[14]Probability distribution function is a sample distribution in either $m_{\rm EC}$ or ΔE

of the blinded region. This fit is done simultaneously in both $m_{\rm EC}$ and ΔE in the 'Fit Box' defined as:

$$1.572\,{\rm GeV} < m_{\rm EC} < 1.950\,{\rm GeV}$$
$$-0.165\,{\rm GeV} < \Delta E < 0.150\,{\rm GeV}$$

Figure 4.8 shows the fits of $m_{\rm EC}$ and ΔE. The pink shows the signal distribution, the black the data and the blue and red the Bhabha and $\tau\tau$ respectively contribution respectively. Once PDF_{bkg} is determined, the number of background events inside the signal region, $N_{2\sigma}^{data}$, is estimated as:

$$N_{2\sigma}^{data} = \frac{\int_{2\sigma} PDF_{bkg}}{\int_{FitBox-3\sigma} PDF_{bkg}} \times N_{FitBox-3\sigma}^{data}$$

where $\int_{2\sigma}$ and $\int_{FitBox-3\sigma}$ are integrals over the 2σ signal region and the unblinded portion of the fit box respectively. This procedure is then repeated fitting instead to the MC background sample. Table 4.8 shows the number of events and expected 90% CL upper limit for the final optimization fit under the assumption there is no signal. To confirm the validity of the fit, table 4.9 compares the fit (expected) number of events to the actual (observed) number of MC events in the fit box outside of the signal region.

		Using MC			Using Data		
	Efficiency	Events		Upper Limit	Events		Upper Limit
		Observed	Expected	Expected	Observed	Expected	Expected
$\tau^{\pm} \to e^{\pm}\,\gamma$	3.91%	0	0.94 ± 0.18	$0.86{\cdot}10^{-7}$	Blinded	1.63 ± 0.25	$0.98{\cdot}10^{-7}$

Table 4.8: Observed & expected events along with the expected Upper Limits using MC & Data.

Decay modes	# of events	-9σ	-5 σ	0	+5 σ	+9 σ
$\tau^{\pm} \to e^{\pm}\,\gamma$	Observed	2	1	Blinded	2	2
	Expected	1.17±0.18	1.36±0.21	1.63±0.25	1.90±0.30	2.08±0.33

Table 4.9: The number of observed and the expected data events obtained from the fit to $m_{\rm EC}$-ΔE distributions outside the signal box of the Fit Box. The number of events within 2σ ellipses shifted by ± 5 σ and ± 9 σ in $m_{\rm EC}$ from the signal box in $m_{\rm EC}$-ΔE plane are shown.

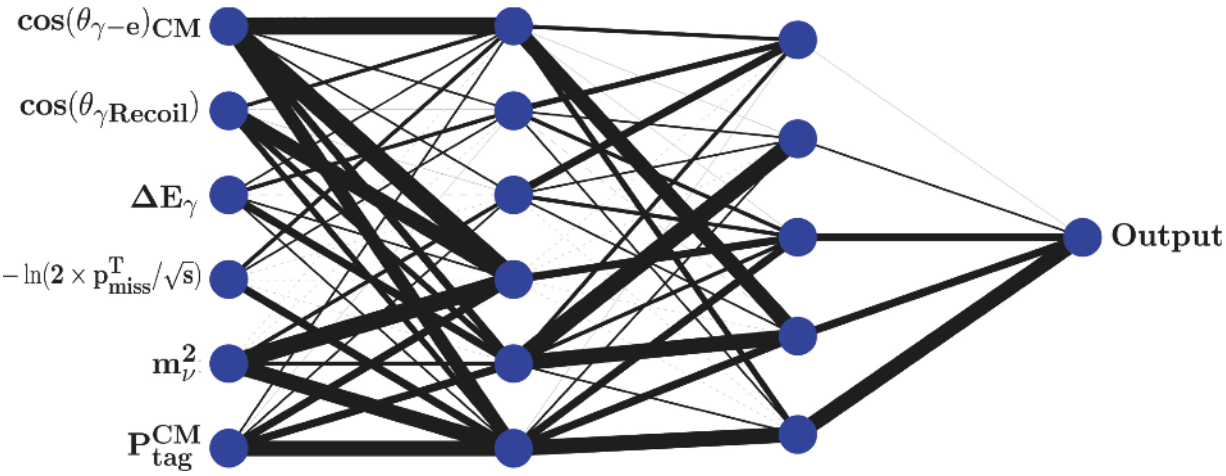

(a) Diagram of the neural network structure. Neurons, shown in blue, output a linear combination of their weighted inputs, shown as black lines.

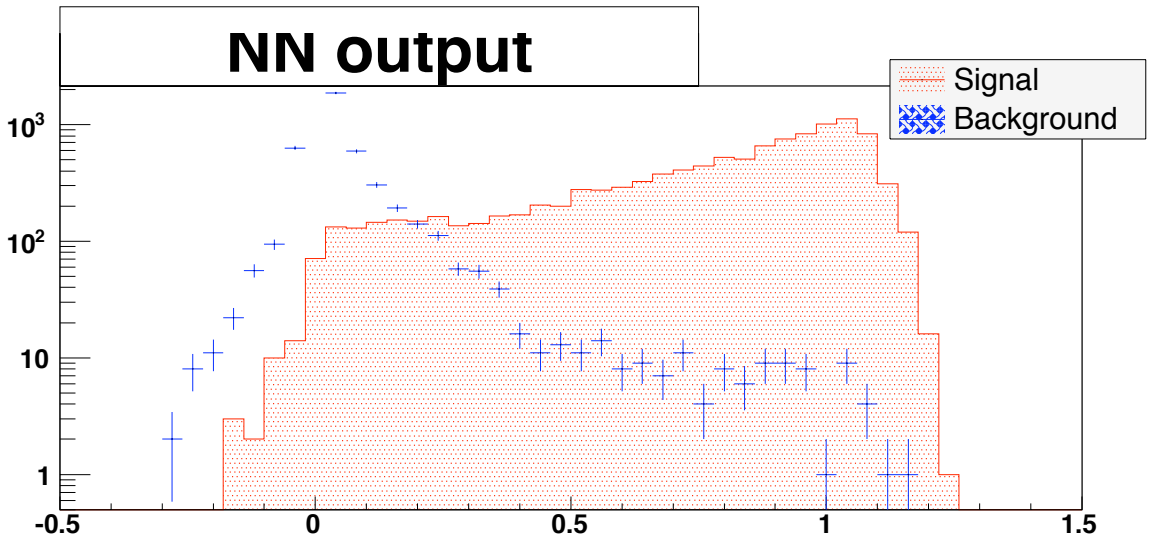

(b) Plot of neural net response to e-tag MC background and MC signal.

Figure 4.6

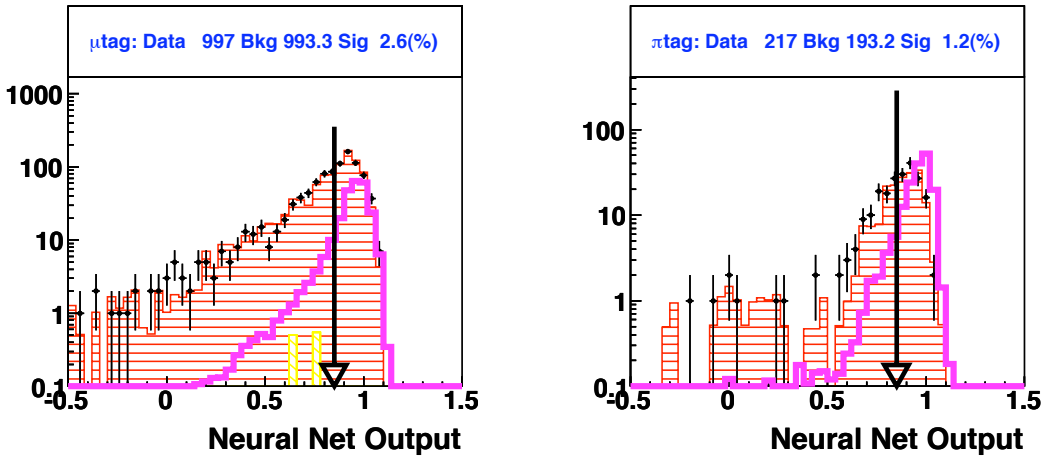

(a) μ-tag

(b) π-tag

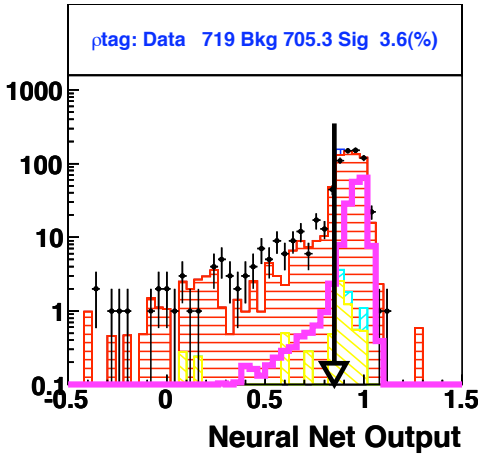

(c) ρ-tag

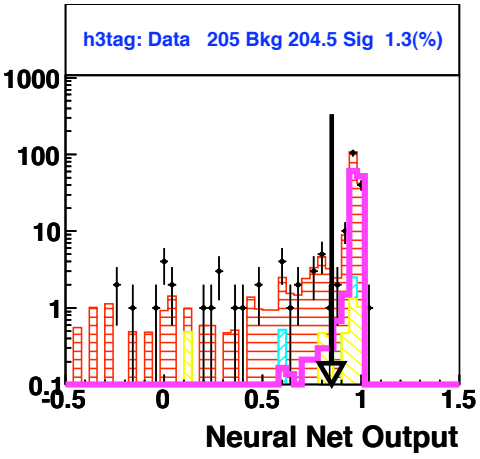

(d) $3h$-tag

Figure 4.7: Neural network output by tag.

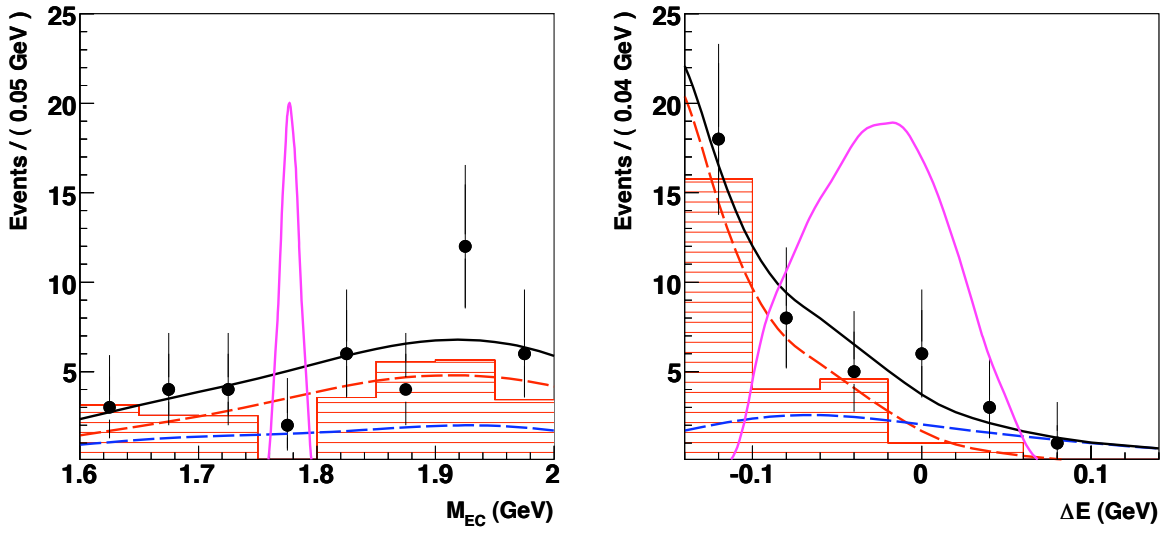

(a) (b)

Figure 4.8: Fitted distributions for m_{EC} and ΔE. The signal distribution is in pink, data in black and Bhabha/$\tau\tau$ in blue/red.

Chapter 5

Systematic Studies

The 90% CL upper limit on the $\tau^{\pm} \to e^{\pm}\,\gamma$ branching ratio is:

$$\mathcal{B}_{90\%CL}(\tau^{\pm} \to e^{\pm}\,\gamma\,) = \frac{N^{90\%CL}_{signal}}{2N_{\tau^+\tau^-}\epsilon}$$

$\mathbf{N^{90\%CL}_{signal}}$	Number of signal events for Feldman-Cousins 90% CL UL [8] assuming no signal
$\mathbf{N}_{\tau\tau}$	number of τ-pairs studied
ϵ	signal selection efficiency

Systematic uncertainty on both $N_{\tau\tau}$ and ϵ must be evaluated.

The systematic uncertainty on the luminosity and $\tau\tau$ cross-sections are 0.9% [25] and 0.3% [26] respectively. This gives a systematic uncertainty of 1.0% on $N_{\tau\tau}$.

The systematic error associated with ϵ arise from discrepancies between MC simulated events and data. The selection procedure introduces a number of systematic errors in the efficiency:

1. Trigger and background filter efficiency

   An inefficiency arises from application of the trigger and background filters. Table 5.1 shows the effects of application of the L3Trgger and BGF to the signal efficiency in the GSB. Application of L3 trigger and BGF tag on the final selection reduces the efficiency from 8.64% to 8.08% – a relative inefficiency of

6.5%. From table 4.7 after the selection is complete there are 1389 data and 1423 MC. Hence the systematic uncertainty in modeling is assigned a value of (Data - MC)/(Data) = 2.4%. Thus this inefficiency contributes $0.024 \cdot 6.5\% = 0.16\%$ to the systematic error on ϵ.

Selection Requirement	ϵ
All Reqs except L3Trig & BGFTAG	8.64
All Reqs except BGFTAG	8.63
All Reqs	8.08

Table 5.1: Final efficiency for all events when applying requirements last on L3 trigger and background filters.

2. Tracking reconstruction efficiency

   The uncertainty due to tracking reconstruction efficiency for 'GoodTracksLoose' is 0.17% per track [27]. Thus, the contributions to the systematic uncertainty are 0.34% and 0.68% for 11 and 13 topologies respectively. Weighting these efficiencies by their fraction of the data set yields a 0.4% contribution to the systematic error.

3. Neutral cluster reconstruction efficiency

   A study of photon reconstruction efficiency has not be studied in detail. A result for π^0 efficiency [28] allows us to estimate that of the photon. Since $\pi^0 \rightarrow \gamma\gamma$ dominates, $\epsilon_{\pi^0} \approx \sqrt{\epsilon_\gamma}$ is a reasonable approximation. This gives $\sigma_\gamma \approx \frac{\sigma_{\pi^0}}{2\sqrt{\epsilon_{\pi^0}}}$. With a 3% π^0 efficiency uncertainty from [28] and an overestimate of $\epsilon_{\pi^0} = 1$, this gives $\sigma_\gamma \approx 1.5\%$

4. Electron Selector PID error

   The entire analysis is re-run using different PID selectors for the signal electron

track. Table 5.2 shows the results of this study. The PID systematic error is taken to be 1.7%, the variance of the signal efficiencies between the 5 different PID selectors.

bit	e PID Selector	Signal Efficiency (%)	MC		Data	
		in 2σ ellipse	Upper Limit (10^{-7})	Predicted	Upper Limit (10^{-7})	Expected
3	Micro.Tight	3.94	1.08	2.3±0.3	1.16	3.0±0.4
4	Micro.VeryTight	3.74	0.88	0.8±0.2	1.00	1.5±0.2
5	LH.Tight	3.82	0.86	0.9±0.2	0.97	1.4±0.2
8	KM.Loose	3.91	0.87	1.0±0.2	0.98	1.6±0.3
9	KM.Tight	3.85	0.87	1.0±0.2	0.96	1.4±0.2

Table 5.2: Optimized NN Selection for different e PID selectors for $\tau^{\pm} \to e^{\pm}\,\gamma$ search.

5. Neural network variable modeling

   The neural net contribution to the systematic error is evaluated by individually substituting each of the neural net variables with their GSB signal value. The effect of this is to remove the influence of that variable on the analysis.

   Another substitution is formed, but the variable is instead replaced by a shifted mean of Mean_{SIGNAL} - (Mean_{DATA} - Mean_{MC}). The resulting shift in signal efficiency shows the sensitivity of the neural net to a shift as large as the data/MC discrepancy.

   The uncertainty on the signal efficiency is taken to be the percentage difference between the two substituted values. The effect of this study is shown in Appendix D. The systematic error is very conservatively taken as the maximum variation at 2.7% for $-\ln(2 \times p^{T}_{miss}/\sqrt{s})$ in the π-tag.

6. Signal track momentum and photon energy resolution

   Tracking and calorimetry errors can effect the position and width (energy resolution) of the signal box. This contribution to the efficiency systematic is determined by rerunning the analysis with a shifted or stretched signal box.

The ΔE and $m_{\rm EC}$ peaks are shifted by $\pm 4\,$MeV and the resolutions are modified by $\pm 1\,$MeV. This effect is overestimated by adding the resultant changes in the efficiency in quadrature to give a systematic of 7.0%.

7. Beam energy scale

   Systematic uncertainties in the beam energy of $\pm 2\,$MeV are possible [29]. Should the beam energy increase (decrease), the result is a decrease (increase) in $\Delta E = E - E_B$ and an increase (decrease) in $m_{\rm EC} \approx \sqrt{E_B^2 - p^2}$. Hence a study employing anti-correlated shift in the GSB was done. The relative changes in the signal efficiency were added in quadrature giving a contribution to the overall systematic of 0.8%.

Table 5.3 shows the results of the systematic studies. The overall systematic uncertainty in the branching fraction is 8.1%.

Systematic Influence on the Signal Efficiency $\tau^{\pm} \to e^{\pm}\,\gamma$	Rel. Error (%)
1. Trigger and BGFilter efficiency	1.7
2. Tracking reconstruction efficiency	0.4
3. Neutral cluster reconstruction efficiency	1.5
4. Electron selector PID error	1.7
5. NN variable modelling	2.7
6. Signal Track and photon energy scale	7.0
7. Beam energy scale and spread	0.8
$N_{\tau\tau}$ uncertainty	1.0
Total	8.1

Table 5.3: Relative Systematic errors (%) associated with the signal efficiency and number of τ pairs.

Chapter 6

Results

6.1 Unblinded Results

Once the optimization procedure is complete and a stable, lowest prediction for the UL is achieved, the data may be unblinded.

Figures 6.1a and 6.1b show the unblinded event distributions in $m_{\rm EC}$ vs ΔE for background and data respectively. No events are observed within the signal region; hence, there is no evidence for signal within the data. A branching ratio may not be

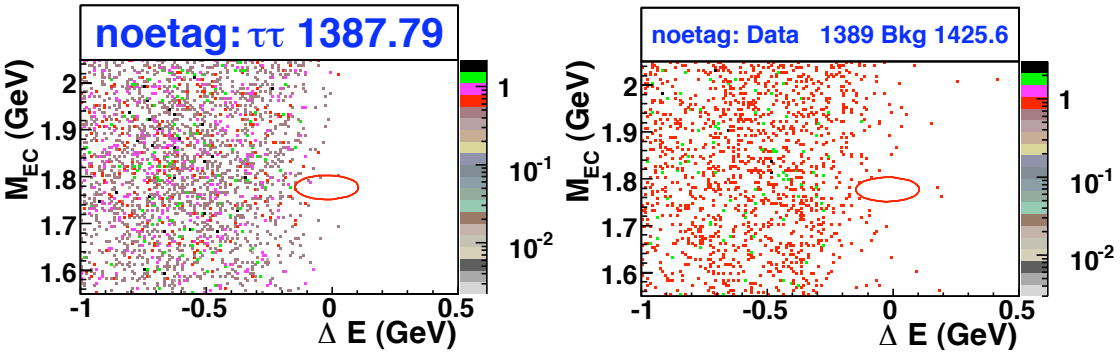

(a) Unblinded background $m_{\rm EC}$ vs ΔE (b) Unblinded data $m_{\rm EC}$ vs ΔE

Figure 6.1

determined for $\tau^{\pm} \to e^{\pm}\,\gamma$.

From table 4.8, the expected number of background events within the signal region is 1.6 ± 0.3. Using the method of Feldman and Cousins [8], an upper limit on the branching ratio may be calculated. A iterative numerical algorithm, POLE [30], is employed to determine the Feldman-Cousins upper limit including uncertainties. Including the signal efficiency of 3.9% (Table 4.7), using $N_{\tau^+\tau^-} = 517.184$ million and including the 8.1% systematic uncertainty, POLE gives:

$$\boxed{\mathcal{B}_{90\%CL}(\tau^{\pm} \to e^{\pm}\,\gamma\,) = 3.3 \times 10^{-8}}$$

This is a factor of three improvement over the previous UL that was placed by *BABAR* at 1.1×10^{-7} [2]. This improvement may be used to constrain some parameters of the SUSY model mentioned in Section 2.4. Examining Figure 2.4a, the improvement made by this study does little to constrain the mixing angle in this case. Some phases and magnitudes are ruled out. More interesting is the constraint placed upon the case depicted by Figure 2.4b, the case where M_0 and $M_{1/2}$ are significantly smaller than the first case. Most phases are ruled out for $|\theta| > 1$.

6.2 Summary

No evidence was found for the decay $\tau^{\pm} \to e^{\pm}\,\gamma$ within the completed *BABAR* data set. A 90% confidence level upper limit was placed on the branching fraction of 3.3×10^{-8}. This result is a factor of three improvement over the previous best limit [2]. This result allows for some constraint on the parameter θ_1, and the soft SUSY breaking parameters M_0 and $M_{1/2}$ within an mSUGRA based SUSY model.

Bibliography

[1] B. Aubert et al. Search for lepton flavor violation in the decay $\tau^{\pm} \rightarrow e^{\pm}\gamma$. *Physical Review Letters*, 96(4):041801, 2006.

[2] C. Amsler et al. (Particle Data Group). The review of particle physics. *Physics Letters B667, 1*, 2008.

[3] Jr. Davis, Raymond, Don S. Harmer, and Kenneth C. Hoffman. Search for neutrinos from the sun. *Phys. Rev. Lett.*, 20:1205–1209, 1968.

[4] Y et al. Fukuda. Measurements of the solar neutrino flux from super-kamiokande's first 300 days. *Phys. Rev. Lett.*, 81(6):1158–1162, Aug 1998.

[5] SNO Collaboration. Measurement of the rate of nu_e + d –> p + p + e^- interactions produced by 8b solar neutrinos at the sudbury neutrino observatory. *Physical Review Letters*, 87:071301, 2001.

[6] R. E. Shrock B. W. Lee. *Phys. Rev. D*, 16:1444, 1977.

[7] Ernesto Arganda and María J. Herrero. Testing supersymmetry with lepton flavor violating tau and mu decays. *Physical Review D (Particles and Fields)*, 73(5):055003, 2006.

[8] Gary J. Feldman and Robert D. Cousins. A unified approach to the classical statistical analysis of small signals. *Physical Review D*, 57:3873, 1998.

[9] P. F. Harrison and H. R. Quinn ed. The *BABAR* physics book: Physics at an asymmetric *b* factory, 1997.

[10] BaBar Collaboration. Babar website: http://www.slac.stanford.edu/bfroot. 2008.

[11] The BABAR Collaboration. The babar detector. *NUCL.INSTRUM.METH.A*, 479:1, 2002.

[12] BABAR Collaboration. Babar technical design report. 1995.

[13] M. Kocian. Performance and calibration of the crystal calorimeter of the babar detector. *Proc. 10th Int. Conf. Calorimetry in Particle Physics (CALOR 2002)*, pages 167–174, 2002.

[14] B. Aubert et al. The BaBar detector. *Nucl. Instrum. Meth.*, A479:1–116, 2002.

[15] R. Bartoldus. et al. Trigger and filter document for run1. *BaBar Analysis BaBar Analysis Document 194*, 2002.

[16] R. J. Sobie E. Torrence O. Igonkina S. Banerjee, M. Roney. Cm2 skims for $e^+e^- \to \mu^+\mu^-$ and $e^+e^- \to \tau^+\tau^-$ events (tauqed2). *BaBar Analysis Document 760.*

[17] S. Agostinelli et al. (GEANT4 Collaboration). *Nucl. Instum. Methods Phys. Res.*, Sect. A 506:250, 2003.

[18] B. Aubert et al. (BaBar Collaboration). *Nucl. Instum. Methods Phys. Res*, Sect. A 489, 1, 2002.

[19] B. F. Ward S.Jadach and Z. Was. *Comput. Phys. Commun*, 130:260, 2000.

[20] R. Decker S. Jadach, Z. Was and J.H.Kuhn. *Comput. Phys. Commun.*, 76:361, 1993.

[21] T.Sjotrand. *Comput. Phys. Commun.*, 82(74), 1994.

[22] D. J. Lange. *Nucl. Instum. Methods Phys. Res.*, Sect. A 462:152, 2001.

[23] R. A. Fisher. *Annals of Eugenics*, 7:179, 1936.

[24] Christophe Delaere. Root tmultilayerperceptron. 2008.

[25] C. Touramanis R. Gamet, R. .J. Parry. Luminosity measurement for run i and ii using sp4 simulation. *BaBar Analysis Document*, 535, 2003.

[26] Swagato Banerjee, Bolek Pietrzyk, J. Michael Roney, and Zbigniew Was. Tau and muon pair production cross sections in electron-positron annihilations at sqrt(s) = 10.58 gev. *Physical Review D (Particles and Fields)*, 77(5):054012, 2008.

[27] Herve Choi. Tracking efficiency task force.

[28] Naisbit M. Roodman A. Allen M., Banerjee S. A study of pi0 efficiency. *BaBar Analysis Document*, 870, 2004.

[29] R. Waldi G. Wagner. *BaBar Analysis Document*, 421, 2002.

[30] Jan Conrad, O. Botner, A. Hallgren, and Carlos Perez de los Heros. Including systematic uncertainties in confidence interval construction for Poisson statistics. *Phys. Rev.*, D67:012002, 2003.

Appendix A

Energy Constrained Mass – m_{EC}

The energy constrained mass (m_{EC}) is the mass of the e, γ system calculated using momenta that are obtained through a kinematic fit with the energy constrained to the beam energy. This fit is performed at the skim level.

Within the signal region m_{inv} and ΔE for signal MC are highly correlated. Figure A.1 (left) shows m_{inv} vs ΔE for signal MC in the signal region. It is advantageous to use two variables which have a low correlation such that two independent measurements identify the signal. Figure A.1 (right) shows m_{EC} vs ΔE and indicates they are much less correlated (0.0845) than m_{inv} (0.6944). m_{EC} provides a better mass resolution and also has a low correlation with ΔE making it a good choice for this analysis.

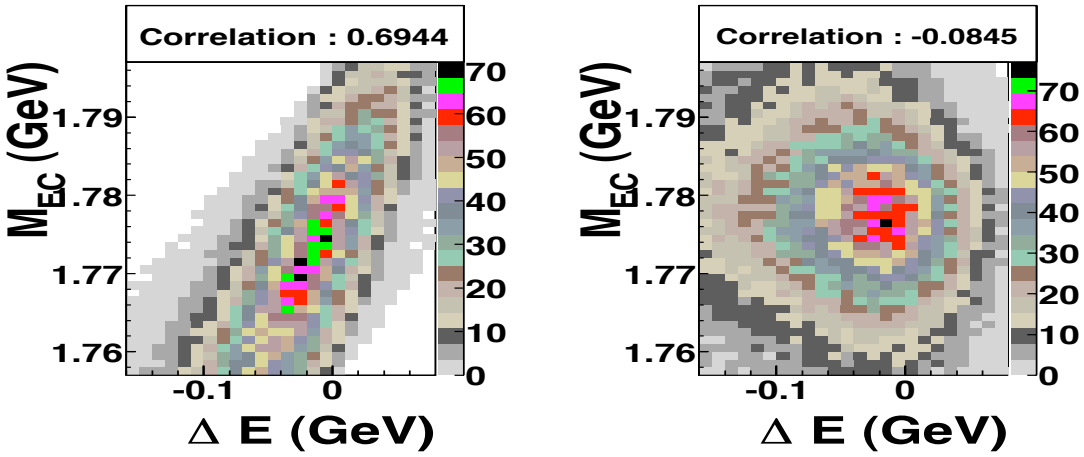

Figure A.1: $\tau^{\pm} \to \mu^{\pm}\gamma$: Correlations for m_{inv} vs ΔE (left) and $m_{\rm EC}$ vs ΔE (right) for for signal MC.

Appendix B

Pseudomass

The tag-side pseudomass is the calculated τ mass assuming the neutrino is massless and colinear with the τ. Consider the decay $\tau \rightarrow h\nu$ where $h = \pi, K$. In this case we have:

$$\mathrm{m}_\tau^2 = E_\tau^2 - p_{tot}^2 = (E_\tau)^2 - (p_\nu + p_h) \cdot (p_\nu + p_h) \tag{B.1}$$

$$= E_\tau^2 - [E_\nu^2 + p_h^2 + 2E_\nu |p_h| cos(\theta)] \tag{B.2}$$

$$= E_\tau^2 - [(E_\tau - E_h)^2 + p_h^2 + 2(E_\tau - E_h)|p_h| cos(\theta)] \tag{B.3}$$

$$= m_h^2 + 2(E_\tau - E_h)(E_h - |p_h| cos(\theta)) \tag{B.4}$$

where θ is the angle between the neutrino and h. With the assumption that the neutrino is co-linear with the τ we have $\theta = 0$ giving:

$$m_{tag}^{pseudo} = \sqrt{m_h^2 + 2(E_\tau - E_h)(E_h - p_h)} \leq m_\tau \tag{B.5}$$

Examining equation B.5 we can see that if $E_h \simeq p_h$ then the second term is small

and we have $m_{tag}^{pseudo} \approx m_h$. This is the case for high-energy, low mass h, such as in the π-tag in cut #7. For more complicated 3-prong geometries, the pseudomass more accurately approximates the τ mass as the neutrino is less energetic. The useful characteristic of the pseudomass is that it has a hard cutoff at the τ mass. Hence any events with higher pseudomass than $m_\tau \approx 1.777\,\text{GeV}$ are likely not from τ pairs.

Hence the pseudomass is useful in cutting out non-τ decays on the tag-side.

Appendix C

Neural Net Variables

- $\mathbf{P_{tag}^{CM}}$: total tag side momentum in CM.

- $\mathbf{m_{\nu}^2}$: tag-side neutrino mass squared.

- $-\ln(\mathbf{2} \times \mathbf{p_{miss}^T}/\sqrt{\mathbf{s}})$: log missing transverse momentum divided by beam energy

- $\mathbf{cos}(\theta_{\gamma-\mathbf{e}})_{\mathbf{CM}}$: angle between signal photon and signal electron in CMS frame

- $\mathbf{cos}(\theta_{\gamma\mathbf{Recoil}})$: angle between signal and tag tracks in the signal γ zero momentum frame

- $\mathbf{\Delta E}_{\gamma}$: Figure C.1 shows an event with signal photon, signal track and tag-side system. We then define:

$$\frac{\Delta E_\gamma}{\sqrt{s}} \equiv \frac{E_\gamma^{CM}}{\sqrt{s}} - \frac{|\sin(\theta_1+\theta_2)|}{\sin\theta_1+\sin\theta_2+|\sin(\theta_1+\theta_2)|} \sim 0$$

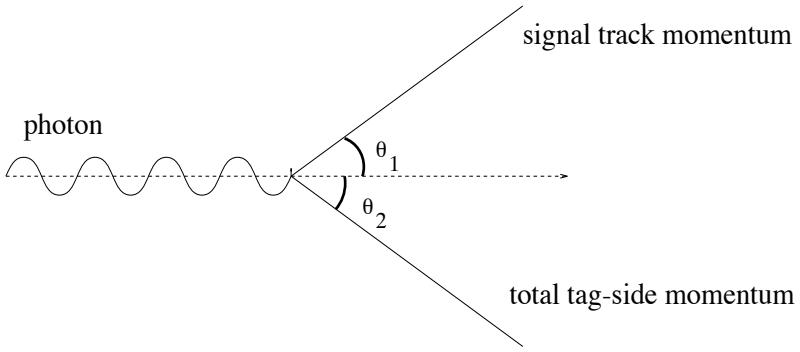

Figure C.1: Reconstructing the photon energy in an e^+e^-annihilation with centre-of-mass energy $= \sqrt{s}$, assuming the direction of photon, signal track momentum and total tag-side momentum.

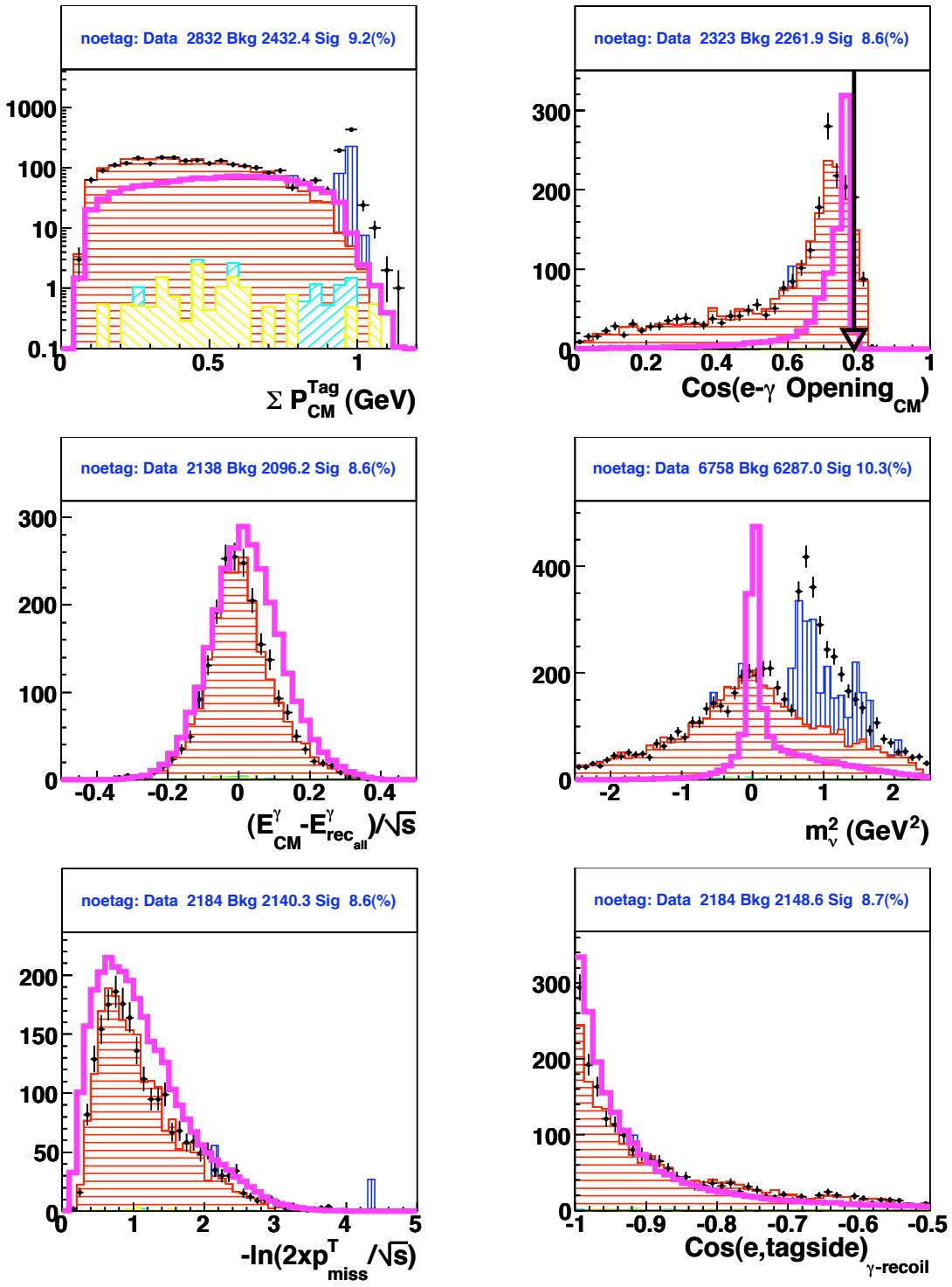

Figure C.2: The six neural network input variables

Appendix D

μ-tag	Signal Mean	(Signal + Data - MC) Mean	Change in Efficiencty (%)
none	3.91	3.91	0.00
P_{tag}^{CM}	3.20	3.20	0.03
m_{ν}^2	3.90	3.91	0.35
$-\ln(2 \times p_{miss}^T/\sqrt{s})$	3.67	3.67	0.05
ΔE_{γ}	3.91	3.91	0.01
$cos(\theta_{\gamma Recoil})$	3.92	3.90	0.53
$cos(\theta_{\gamma-e})_{CM}$	2.85	2.85	0.03

π-tag	Signal Mean	(Signal + Data - MC) Mean	Change in Efficiencty (%)
none	3.91	3.91	0.00
P_{tag}^{CM}	3.67	3.69	0.36
m_{ν}^2	3.86	3.86	0.00
$-\ln(2 \times p_{miss}^T/\sqrt{s})$	3.70	3.81	2.70
ΔE_{γ}	3.91	3.91	0.01
$cos(\theta_{\gamma Recoil})$	3.91	3.91	0.02
$cos(\theta_{\gamma-e})_{CM}$	3.37	3.37	0.00

ρ-tag	Signal Mean	(Signal + Data - MC) Mean	Change in Efficiencty (%)
none	3.91	3.91	0.00
P_{tag}^{CM}	3.91	3.91	0.01
m_{ν}^2	2.70	2.67	0.95
$-\ln(2 \times p_{miss}^T/\sqrt{s})$	3.90	3.89	0.36
ΔE_{γ}	3.91	3.91	0.00
$cos(\theta_{\gamma Recoil})$	3.90	3.90	0.01
$cos(\theta_{\gamma-e})_{CM}$	3.55	3.55	0.07

3h-tag	Signal Mean	(Signal + Data - MC) Mean	Change in Efficiencty (%)
none	3.91	3.91	0.00
P_{tag}^{CM}	3.91	3.91	0.00
m_{ν}^2	3.73	3.73	0.04
$-\ln(2 \times p_{miss}^T/\sqrt{s})$	3.83	3.84	0.25
ΔE_{γ}	3.90	3.90	0.15
$cos(\theta_{\gamma Recoil})$	3.90	3.90	0.06
$cos(\theta_{\gamma-e})_{CM}$	3.84	3.84	0.04

Figure D.1: Effect on the signal efficiencies when replacing net variable input with $Signal + Data - MC$ mean for $\tau^{\pm} \to e^{\pm}\,\gamma$.